

Time-dependent oscillating viscoelastic Rayleigh-Bénard convection: Viscoelastic kinetic energy budget analysis

Xin Zheng


College of Shipbuilding Engineering, Harbin Engineering University, Harbin 150001, China

M'hamed Boutaous * and Shihe Xin

Univ. Lyon, CNRS, INSA-Lyon, Université Claude Bernard Lyon 1, CETHIL UMR5008, F-69621, Villeurbanne Cedex, France

Dennis A. Siginer

Departamento de Ingeniería Mecánica, Universidad de Santiago de Chile, Avenida Libertador Bernardo O'Higgins No. 3363, Estación Central, Santiago, Chile

Weihua Cai 

Laboratory of Thermo-Fluid Science and Nuclear Engineering, Northeast Electric Power University, Jilin 132012, China



(Received 14 June 2022; accepted 5 January 2023; published 21 February 2023)

The time-dependent oscillating convection leading to the formation of reverse flowing cells is a special phenomenon induced by viscoelasticity in the Rayleigh-Bénard convection (RBC). The causes and the evolution of this overstability problem have not yet been investigated in-depth. Numerical simulations of the viscoelastic Rayleigh-Bénard convection (VRBC) have been conducted in this work with viscoelastic working fluids abiding by the nonlinear Phan-Thien-Tanner (PTT) constitutive structure in two-dimensional cavities. To understand the impact of the nonlinearity and the rheological parameters on the mechanism of the regular reverse flow numerical simulations have been performed over the range of $\beta = (0.1, 0.2)$ (where $\beta = \mu_s/\mu_0$, μ_s is the solvent viscosity, $\mu_0 = \mu_s + \mu_p$ is sum of solvent viscosity μ_s and polymer viscosity μ_p) and Weissenberg number ($We \in [0.075, 0.25]$), using an in-house finite-difference code. The remaining constitutive parameters of the (PTT) fluid representing elongational and slippage characteristics of the fluid were kept fixed at $\epsilon = 0.1$ and $\xi = 0.05$, respectively. A viscoelastic kinetic-energy budget method was used to analyze the energy transport in this time-dependent reverse flow process. An original parametric analysis is developed to gain an insight into the dynamics of the reversal flow observed recently in our work, Zheng *et al.* [*Phys. Rev. Fluids* **7**, 023301 (2022)], as well as observed by Park and Ryu [*Rheol. Acta* **41**, 427 (2002)] and Lappa and Boaro [*J. Fluid Mech.* **904**, A2 (2020)]. The emergence of the reversal convection can be explained by the transfer of potential energy between flow and fluid elasticity during the reversal process. The existence of time phase differences of different potentials in the evolution drive this potential-energy transfers.

DOI: [10.1103/PhysRevFluids.8.023303](https://doi.org/10.1103/PhysRevFluids.8.023303)

*mhamed.boutaous@insa-lyon.fr

I. INTRODUCTION

The Rayleigh-Bénard convection (RBC) in a cavity consists in a fluid heated from top and cooled from the bottom generating a flow caused by thermal buoyancy. As one of the most fundamental and ubiquitous physical phenomena in nature and industrial processes, RBC has been extensively studied for more than a hundred years [1,2]. A stationary RBC system will lose its hydrodynamic stability when the buoyancy force exceeds its viscous dissipation which maintains the stability of the system, and laminar convection will take place [3,4]. The Rayleigh number $Ra = \alpha g \Delta T H^3 / \nu \kappa$ (where $\Delta T = T_2 - T_1$ is the temperature difference between the bottom and top and $\kappa = k / \rho_0 C_p$ is thermal diffusivity) represents the ratio of the buoyancy force and the viscous forces. When Ra increases further, the stable laminar convection cannot be maintained any longer and the turbulent thermal convection starts, Lohse and Xia [5]. The flow pattern selection or bifurcation on the transition from stationary to chaos is extensively documented [2].

Polymeric fluids exhibit a very strong viscoelastic behavior. The long-chain macro-molecular structure of the polymer suspended in a Newtonian fluid solvent will confer more complexity to the (viscoelastic Rayleigh-Bénard convection, or VRBC) compared with the Newtonian Rayleigh-Bénard convection (NRBC) [6], such as elastic instability [7] and enhancement or reduction heat transport [8,9]. As an important facet of the elastic instability of VRBC, the elasticity-induced oscillations were known for decades. Most of the efforts in the past on this problem focused on the influence of the rheological parameters on pattern selection, especially on the critical Rayleigh number Rac for convection onset through linear instability analyses [10–17]. There are a few studies that investigated some facets of the flow behavior such as the magnitude of the convection amplitude in oscillating VRBC via weakly nonlinear stability analyses [18–21].

The advent of more sophisticated and accurate constitutive models since the early pioneering work of Green III [10] using the upper-convected Maxwell model motivated further studies on the oscillating VRBC [11,22,23]. Park and Lee [24] pointed out the existence of different convection onset points in VRBC depending on the elasticity of the fluid through a linear instability analysis. The time-dependent oscillating convection onset takes place in strongly elastic (extraordinary conditions) VRBC and the steady convection onset is associated with weakly elastic VRBC, which is similar to the onset in the Newtonian cases. This result specifically reinforces the point of Larson [25], namely, “viscoelastic effects are unimportant in the linear stability of the Rayleigh-Bénard flow, except perhaps under extraordinary conditions,” meaning under a large temperature difference or a very substantial elasticity or small-geometry configuration. The oscillation period can be very long because the viscoelastic fluid tends to acquire the properties of an inelastic Newtonian fluid as its elasticity becomes negligibly small. Unlike the randomly oscillating NRBC, the oscillating process in VRBC shows a spatial and temporal periodicity and exhibits a strong correlation with the rheological parameters of the viscoelastic fluid. This phenomenon was also experimentally observed in RBC affected by magnetic or electric fields [26,27]. Park and Ryu [12,20] and Park *et al.* [28] systematically investigated the oscillating VRBC in infinite and two-dimensional (2D) enclosures space via linear and nonlinear stability analyses. They worked with a general viscoelastic constitutive model and clarified the relationships between Rac and (β, We) in the case of an infinite horizontal cavity. Their results show that Rac for convection onset increases as We decreases or β increases, and the steady convection onset is replaced by the oscillating reversal convection by We increases and/or β decreases [13,29]. Similar results were also obtained through a weakly nonlinear stability analysis by Kovalevskaya and Lyubimova [30] and Bhadauria and Kiran [31]. They studied the effect of gravity modulation on the over-stability of VRBC. The effect of the relaxation time and the retardation time on the heat transfer capacity and on the Rac was investigated. Both Rac and the heat transfer capacity strongly correlate with the relaxation and retardation times.

Oscillating viscoelastic convection was studied experimentally by Kolodner [32]. He investigated the Rayleigh-Bénard convection of a DNA suspension in a ringlike container and observed the oscillating convection. He argues that the oscillations maybe driven by the deformation of the DNA. The experimental work of Métivier *et al.* [33] with elasto-viscoplastic carbopol gels confirms the findings

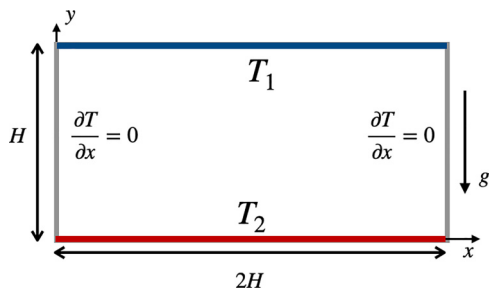


FIG. 1. Computational configuration of aspect ratio $A = 2$.

of the recent studies of the oscillatory VRBC using direct numerical simulations [7,29,34,35]. M etivier *et al.* [33] studied the thermal convection with slip boundary conditions. A very intuitive velocity vector diagram of convection reversal was given for different stresses. However, their results only gave a simplified and superficial account of the regular convection reversal. The view of M etivier *et al.* [33] is that the oscillating convection is related to slip at the wall. However, they do not rule out the role of the fluid elasticity. Thus, clearly the oscillating convection with viscoelastic fluids is still an open problem.

To the best of our knowledge, there is no research reported in the literature explaining how the regular oscillating convection evolves and what triggers and supports reversal in VRBC. The first aim of the present work is to explain the mechanism of convection reversal through a kinetic-energy budget analysis by performing a series of direct numerical simulations on the regular reversal convection in VRBC using an in-house solver. The numerical code to simulate VRBC was detailed in-depth and its capability proven in our recent work [36]. The Phan-Thien-Tanner constitutive model is used to describe the viscoelastic fluid, which introduces two extra rheological parameters ϵ and ξ , fixed in this paper. Some examples of the experimentally determined values of the constitutive constants ξ and ϵ in the literature are for dilute polymeric solutions like low concentration polyethylene (LDPE), $\epsilon = 0.02$ and $\xi = 0.1$ whereas for concentrated polymeric solutions like molten polyethylene (HDPE) $\epsilon = 0.02$ [37]. Other polymeric fluids, such as 5% polyisobutylene (PIB) solutions are characterized by $\epsilon = 0.25$ and $\xi = 0.25$ [38]. The second aim of the present work is to complete the results of our recent work [36]. Details of three-cell flows, the relevant reversal mechanism and the corresponding heat transfer are provided. The rest of the paper is organized as follows: Section II summarizes the numerical approach and procedures. Section III A briefly introduces the process of reversal convection. Sections III B to III D show the effect of rheological parameters (β , We) on Rac as an extension of the previous research (Zheng *et al.* [39]) and present main results on regular oscillating convection in VRBC. Section III E details the results about heat transfer analysis.

II. NUMERICAL PROCEDURES

A. Governing equations and computational model

The VRBC was simulated in a $2 : 1$ cavity, shown in Fig. 1, filled with a viscoelastic fluid, which obeys the constitutive equation of Phan-Thien-Tanner model. In Cartesian coordinate system, x is the horizontal direction perpendicular to the gravity g , y denotes the vertical direction parallel to g . The no-slip boundary condition is imposed on all boundaries. A temperature difference $\Delta T = (T_2 - T_1)$ with ($T_2 > T_1$) was also imposed between two horizontal walls, T_2 and T_1 representing the temperatures on the bottom and top, respectively. There is no heat flux on the vertical walls ($\partial T / \partial x = 0$ at $x = 0$ and $x = 2$).

Total stress $\sigma = \tau_s + \tau_p$ is the sum of the Newtonian solvent contribution $2\mu_s D$ and the viscoelastic polymer contribution τ_p . μ_s is the solvent viscosity and $D = \frac{1}{2}(\nabla u + \nabla u^T)$ is the deformation

rate tensor. The polymeric extra-stress tensor τ_p is described by the constitutive equation:

$$\overset{\nabla}{\tau}_p = -\frac{1}{\lambda}\tau_p + 2\frac{\mu_p}{\lambda}\mathbf{D} - \frac{\epsilon}{\mu_p}\text{tr}(\tau_p)\tau_p - \xi(\mathbf{D}\tau_p + \tau_p\mathbf{D}), \quad (1)$$

where λ is the relaxation time, μ_p is the zero shear rate molecular viscosity, and ϵ and ξ are two constitutive parameters representing respectively the elongational behavior of the long-chains and the slip between polymer molecules and the surrounding continuum. In Eq. (1), the superscript ∇ indicates the contravariant convected time derivative expressed by

$$\overset{\nabla}{\tau}_p = \frac{\partial \tau_p}{\partial t} + (\mathbf{u} \cdot \nabla)\tau_p - \nabla \mathbf{u}^T \cdot \tau_p - \tau_p \cdot \nabla \mathbf{u}. \quad (2)$$

The following scale factors are introduced to nondimensionalize the governing field equations:

$$x^* = \frac{x}{H}, \quad t^* = t \frac{U_c}{H}, \quad \mathbf{u}^* = \frac{\mathbf{u}}{U_c}, \quad T^* = \frac{T - T_0}{T_2 - T_1}, \quad p^* = \frac{p}{\rho_0 U_c^2}, \quad \text{and} \quad \tau_p^* = \frac{\tau_p}{\rho U_c^2},$$

with H being the cavity height and the reference velocity $U_c = \frac{\kappa}{H}\sqrt{Ra}$. To simplify the notation, we drop hereafter (*) from all the dimensionless variables. The dimensionless governing field equations with the Oberbeck-Boussinesq approximation for two-dimensional (2D) VRBC are written as

$$\nabla \cdot \mathbf{u} = 0, \quad (3)$$

$$\frac{\partial \mathbf{u}}{\partial t} + (\mathbf{u} \cdot \nabla)\mathbf{u} = -\nabla p + \beta \frac{Pr}{\sqrt{Ra}} \Delta \mathbf{u} + \nabla \cdot \tau_p + Pr Te_j, \quad (4)$$

$$\frac{\partial T}{\partial t} + (\mathbf{u} \cdot \nabla)T = \frac{1}{\sqrt{Ra}} \Delta T + f2\beta \frac{EcPr}{\sqrt{Ra}} \mathbf{D} : \nabla \mathbf{u} + Ec \tau_p : \nabla \mathbf{u}, \quad (5)$$

$$\begin{aligned} \frac{\partial \tau_p}{\partial t} + (\mathbf{u} \cdot \nabla)\tau_p - \nabla \mathbf{u}^T \cdot \tau_p - \tau_p \cdot \nabla \mathbf{u} = & -\frac{1}{We\sqrt{Ra}} \tau_p + 2\frac{1-\beta}{Ma^2} \mathbf{D} \\ & - \epsilon \frac{\sqrt{Ra}}{(1-\beta)Pr} \text{tr}(\tau_p)\tau_p - \xi(\mathbf{D}\tau_p + \tau_p\mathbf{D}), \end{aligned} \quad (6)$$

where $\mathbf{u} = (u_1, u_2)$ is the velocity field, the \mathbf{e}_j is the unit vector along the j th direction, T is the temperature field, p is the pressure field, and τ is the extra stress tensor. The incompressibility constraint ($\partial \mathbf{u} / \partial \mathbf{x} = 0$) is satisfied. The Prandtl number Pr denotes the ratio of the kinematic viscosity and the thermal diffusivity ($Pr = \mu_0 C_p / k = \nu / \kappa$), the Weissenberg number $We = \lambda \kappa / H^2$ is the ratio of the elastic forces to the viscous forces, the viscoelastic Mach number is defined as $Ma = \sqrt{Ra We / Pr}$. The dimensionless Eckert number $Ec = U_c^2 / (C_p \Delta T)$ expresses the relationship between kinetic energy and the enthalpy, and is used to characterize the influence extent of the heat dissipation. For all the cases investigated in this work, Ec takes on values of the order of $O(10^{-10})$, and the magnitude of the values of $\beta Ec Pr / \sqrt{Ra}$ corresponds to $O(10^{-11})$. These values of Ec are extremely small ($\ll 1$), so that the viscous dissipation and the elastic dispersion can be ignored in the calculations presented in this paper. The boundary conditions are set as follows: the no-slip boundary condition is imposed on all boundaries; the thermal boundary conditions are adiabatic on the vertical walls ($\partial T / \partial x = 0$ at $x = 0$ and $x = 2$); a temperature difference $\Delta T = (T_2 - T_1)$ ($T_2 = 1$ and $T_1 = 0$) is imposed on the horizontal walls, T_2 and T_1 represent the temperatures on the bottom and top, respectively.

We point out that, due to the definition of the reference velocity $U_c = \frac{\kappa}{H}\sqrt{Ra}$ in this paper, the natural way to define We is to use U_c , as has been done by Cheng *et al.* [9]. The drawback of using U_c to define We is that We will change with Rayleigh number. To prevent this We dependency on Ra , a definition of We independent of Ra , $We = \kappa \lambda / H^2$, is used in this paper: for $Ra = 1600$ and $We = 0.1$ in the present work for instance, the equivalent We is $We = 10.58$ in the work by Cheng

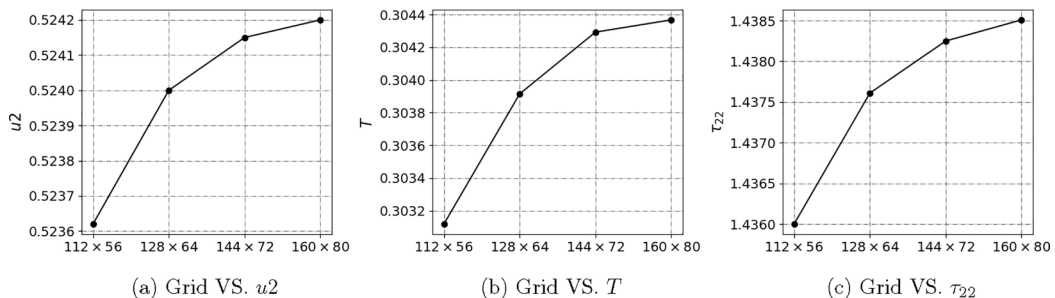


FIG. 2. Grid independence is checked with the parameters $Ra = 1200$, $Pr = 7.0$, $\beta = 0.1$, $We = 0.150$, $\epsilon = 0.1$, and $\xi = 0.05$ and the corresponding convection pattern is time-dependent periodic convection. Maximal values of u_2 , T , and τ_{22} in one time period at the monitoring position $(1, 0.5)$ are used to show the grid independence.

et al. [9], where $U_c = \sqrt{\alpha g H \Delta T}$. We note that the numerical code developed in-house and used in this work is highly efficient for high We , which is another important contribution of the present work.

B. Numerical schemes

The governing equations and proper boundary conditions are solved using an in-house code. A quasilinear treatment of the hyperbolic terms in the linear momentum equation and the viscoelastic constitutive equation was adopted. The capability of this solver to simulate VRBC has been validated in our previous work [36,39,40], where the numerical procedure is detailed. We recall briefly the main features. Velocity-pressure coupling gives rise to the elliptic nature of the governing equations while velocity- τ_p coupling gives rise to the hyperbolic nature of the governing equations. To cope with the hyperbolic nature, a quasilinear treatment of the hyperbolic terms $[(\mathbf{u} \cdot \nabla) - \nabla \cdot \boldsymbol{\tau}_p]$ in the momentum equation and $(\mathbf{u} \cdot \nabla) \boldsymbol{\tau}_p - \nabla \mathbf{u}^T \cdot \boldsymbol{\tau}_p - \boldsymbol{\tau}_p \cdot \nabla \mathbf{u} - 2 \frac{1-\beta}{Ma^2} \mathbf{D}$ in the viscoelastic constitutive equation was adopted. A second-order semi-implicit time scheme is used: the implicit terms are mass conservation, pressure gradient, molecular diffusion, relaxation term, and thermal diffusion; other terms including the quasilinear forms are explicit. Time evolution implemented makes use of the second backward differential formula (BDF2). In space, the second-order central difference is applied to most of the terms except for the quasilinear parts which are treated in the eigenspace of A_i by a high-order upstream central (HOUC) scheme according to the sign of each eigenvalue. A uniform and a staggered grid was used for the spatial discretization and for the velocity-pressure coupling, respectively. The latter is handled by the projection method. In all the simulated cases, the nondimensional numbers and the constitutive constants are fixed as follows: $Pr = 7.0$, $We \in [0.07125, 0.25]$, and $\beta = (0.1, 0.2)$.

Note that the BDF2, well known for solving the Navier-Stokes equations of incompressible viscous fluids, is also applied here due to the fact that the working fluid is incompressible. Also, due to the hyperbolic nature resulted from velocity- τ_p coupling, central differencing schemes cannot be used to treat the quasilinear terms and that the HOUC, similar to the well-known ENO and WENO schemes for hyperbolic equations are applied here although it may not conserve the discrete kinetic energy.

C. Grid-independence verification

The grid independence was tested with the following values of the parameters $Ra = 1200$, $Pr = 7.0$, $\beta = 0.1$, $We = 0.150$, $\epsilon = 0.1$, and $\xi = 0.05$. A small enough time step was chosen $\delta t = 0.001$ not to affect the results. Four grids [122×56 , 128×64 , 144×72 , 160×80] were tested. As shown

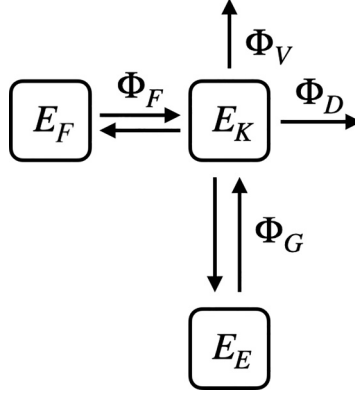


FIG. 3. Energy conversion framework for the VRBC in regular reversal.

in Fig. 2, there is only a very small difference between the grids 128×64 and 160×80 . Thus, the grid with 128×64 nodes was used in all the simulations in this paper.

D. Viscoelastic kinetic-energy budget

We introduce a viscoelastic kinetic-energy budget analysis method in this paper following the ideas of Cheng *et al.* [9] and Li *et al.* [41] who used the kinetic-energy budget method to gain new insight into turbulent VRBC. A understanding of the reversal evolution can be developed by considering the global and local kinetic-energy exchange.

The instantaneous fluid field energy can be split into the components shown in Eq. (7), each one of them denoting local or global-integrated quantities (with operator $\langle \cdot \rangle_\omega$):

$$\frac{dE}{dt} = \Phi_D + \Phi_V + \Phi_G + \Phi_F, \quad (7)$$

where

- (i) $E = \frac{1}{2}u_i u_i$ denotes the kinetic energy;
- (ii) $\Phi_D = -\frac{\partial(pu_j)}{\partial x_j} + \beta \frac{Pr}{\sqrt{Ra}} \frac{\partial^2 E_{ij}}{\partial x_j^2}$ represents the pressure diffusion and molecular viscous transport;
- (iii) $\Phi_V = -\beta \frac{Pr}{\sqrt{Ra}} \frac{\partial u_i}{\partial x_j} \frac{\partial u_i}{\partial x_j}$ represents the viscous dissipation, which describes the work done by a fluid layer on adjacent layers, transformed into heat due to the action of shear forces;
- (iv) $\Phi_G = -\left(\frac{\partial(u_i \tau_{ij})}{\partial x_j} - \tau_{ij} \frac{\partial u_i}{\partial x_j}\right)$ denotes the energy transition between flow structures and polymer microstructures due to the stretching and relaxation behavior of polymer chains, where $\frac{\partial(u_i \tau_{ij})}{\partial x_j}$ and $\tau_{ij} \frac{\partial u_i}{\partial x_j}$ denote the dissipation and interactive impact between flow and polymers, respectively;
- (v) $\Phi_F = PrTe_j u_i$ is buoyancy flux input which describe the work done by the density difference due to the Boussinesq approximation.

The energy conversion distribution map is shown in Fig. 3. There are three forms of energy reservoirs, the kinetic energy E_K , the elastic energy E_E , and the buoyancy potential energy E_B . On the right-hand side of Eq. (7), Φ_G refers only to the energy transfer between flow and polymeric structures, and it does not directly represent the magnitude of the elastic potential energy. To characterize the elastic energy in this convection flow with the viscoelastic whose behavior is described by the PTT model, the component C_{ij} of the deformation tensor \mathbf{C} as the end-to-end moment $\langle (r_i r_j) \rangle$ of the extension of the polymers, modeled as linear spring-dumbbell is used. In this scaling, the equilibrium deformation corresponds to an isotropic distribution with unit end-to-end

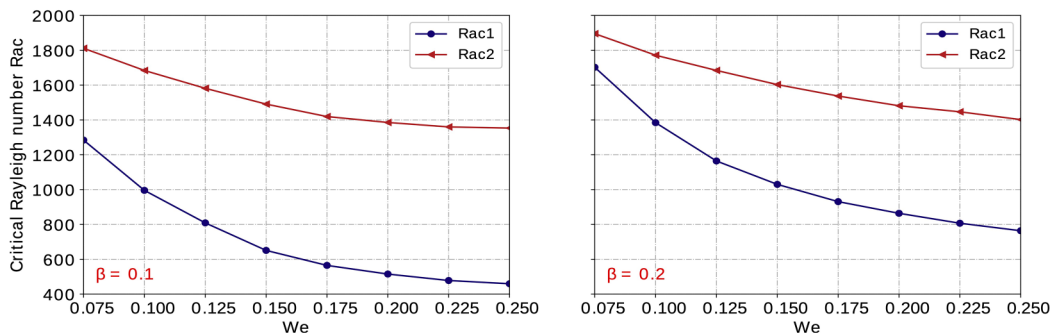


FIG. 4. Critical Rayleigh numbers $Rac1$ and $Rac2$ as a function of We with $\beta = 0.1, 0.2$. The remaining constitutive parameters are fixed at $\epsilon = 0.1$, $\xi = 0.05$. Below $Rac1$ the cavity is in pure conductive and motionless regime, between $Rac1$ and $Rac2$ flow regime is time-dependent, and above $Rac2$ flow regime is steady in the cavity.

displacements [42]. As the relationship between the elastic stress and strain can be expressed by

$$\tau_p = \frac{1 - \beta}{We} (\mathbf{C} - \mathbf{I}), \quad (8)$$

where \mathbf{C} is the polymer deformation tensor and \mathbf{I} is the unit tensor. The elastic energy stored in the polymers is proportional to

$$\frac{1 - \beta}{We} \text{tr}(\tau_p) \sim \left(\frac{1 - \beta}{We} \text{tr}(\mathbf{C}) + \text{constant} \right). \quad (9)$$

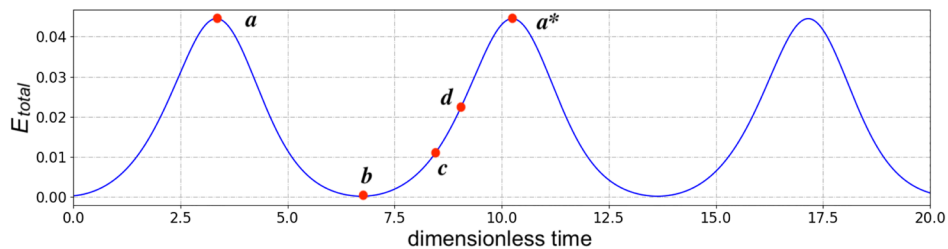
Hence, the total normal elastic stress τ_{ii} will be used to represent the stretching and shrinking energy evolution of the macromolecular structure of the polymer in the viscoelastic flow.

III. RESULTS AND DISCUSSION

For the parameters studied, time-dependent reversal convection sets in at $Rac1$ due to a Hopf bifurcation and ends at $Rac2$ due to a drift-pitchfork bifurcation. The two critical Rayleigh numbers are determined by a less conventional stability analysis based on the fact that the bifurcations are supercritical and that the solution characteristics (solution amplitude for a Hopf bifurcation and solution frequency for a drift-pitchfork bifurcation) are linear with $\sqrt{|Ra - Rac|}$. The linear relationship is extrapolated to the critical point and this allows us to determine the critical Rayleigh number. Details can be found in our previous paper (Zheng *et al.* [39]). The results obtained are displayed in Fig. 4. The regions of Ra between $Rac1$ and $Rac2$ correspond to the regular reversal convection which will be investigated in detail.

A. Time-dependent convection reversal

Periodic convection reversal is depicted in Fig. 5. Figure 5(a) plots the total kinetic energy E_{total} as a function of time and shows a regular periodic behavior. Five particular time points in one kinetic-energy period π are chosen and marked on this curve from $t = a$ to $t = a^*$, a and a^* corresponding to the maximum kinetic energy while $t = b$ corresponds to the minimum. Note that one time period of kinetic energy is only one half of time velocity period. The kinetic energy E , streamline, and temperature T fields corresponding to these five monitoring points are displayed in Figs. 5(b) to 5(k). The reverse behavior takes place at before and close to $t = b$ (E almost equal to zero). The arrows indicate the rotation direction of the cells. Clearly, the reversal arises when the kinetic energy is minimal (point b). The temperature in its evolution exhibits high gradient in the central zone at the beginning of the period, then progressively, the heated zone diffuses into the cold zone and the



(a) Time evolution of total kinetic energy E_{total} and five particular time points.

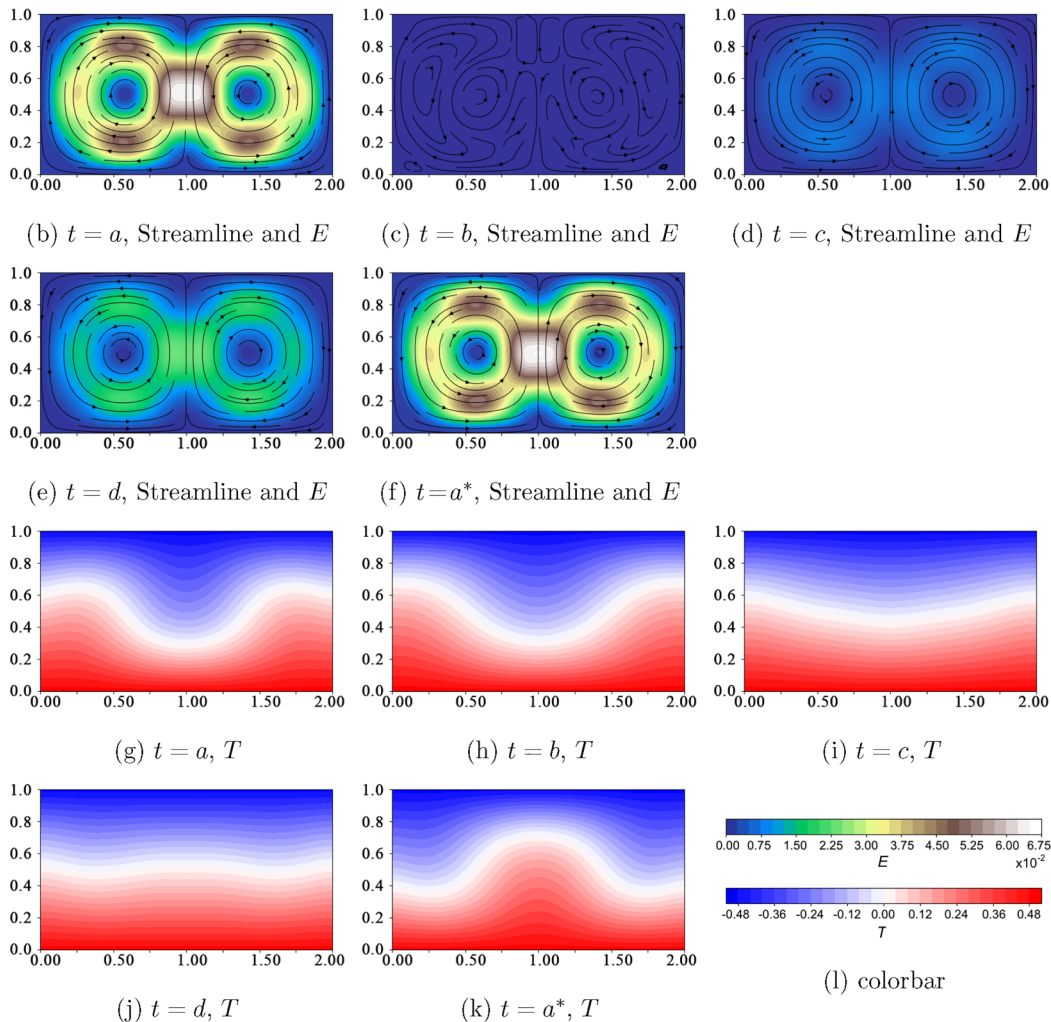


FIG. 5. Time evolution of total kinetic energy E_{total} showing the flow pattern transition of two-cell convection. 2 : 1 cavity filled with a PTT fluid ($Ra = 1200$, $Pr = 7.0$, $\beta = 0.1$, $We = 0.150$, $\epsilon = 0.1$, and $\xi = 0.05$) at the five particular time points indicated in panel (a).

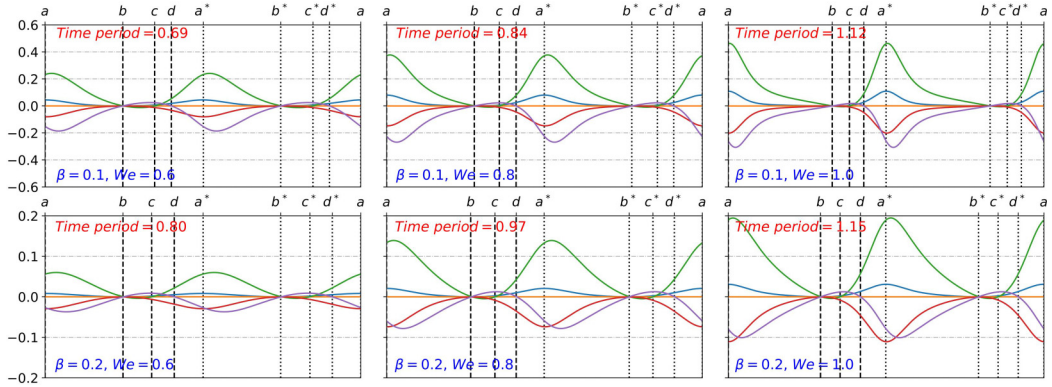


FIG. 6. Different energy evolution in a period corresponding to a complete reversal for $\beta = 0.1$ (top) and $\beta = 0.2$ (bottom) with $We = (0.150, 0.200, 0.250)$ (from left to right), where the time period was normalized graphically. (The green curve) corresponds to buoyancy flux ($\langle \Phi_F \rangle_\Omega$), (the orange curve) corresponds to kinetic diffusion ($\langle \Phi_D \rangle_\Omega$), (the purple curve) corresponds to energy exchange between flow structures and polymer microstructures due to the stretching and relaxation of polymer chains ($\langle \Phi_G \rangle_\Omega$), (the red curve) corresponds to bulk viscous dissipation of kinetic energy ($\langle \Phi_V \rangle_\Omega$), and (the blue curve) corresponds to global kinetic energy ($\langle E \rangle_\Omega$). We fixed $Ra = 1200$, $Pr = 7.0$, $\epsilon = 0.1$, and $\xi = 0.05$.

temperature gradient smooths out before the direction is inverted in the central zone and the cycle continues.

B. Energy transition in viscoelastic Rayleigh-Bénard convection from global view

For the tested cases, the following parameters are used: $Ra = 1200$, $Pr = 7.0$, $\epsilon = 0.1$ and $\xi = 0.05$, $We = (0.1, 0.15, 0.2)$, and $\beta = (0.1, 0.2)$. Figure 6 shows the evolution of each type of the integrated energy ($\langle \cdot \rangle_\Omega$) in dimensionless time in one completed reversal period with varying We . To facilitate the comparison, the time period in each case is rescaled graphically into the same x -coordinate range, and the real time period is written in the right-top of the figure. $\langle \Phi_V \rangle_\Omega$ is negative or almost zero during the reversal process, which agrees with its definition. $\langle \Phi_D \rangle_\Omega$ is almost zero at all times and can be neglected in the process of kinetic-energy transport. $\langle \Phi_F \rangle_\Omega$ is most of the time positive and thus is a globally generating term during the process because it is most of the time positive, which agrees with the fact that RBC is a buoyancy-driven flow. $\langle \Phi_G \rangle_\Omega$ is globally dissipation term because it is most of the time negative.

A half-period of the reversal process (from the time-point with peak kinetic-energy value to next maximum kinetic-energy time-point with opposite velocity direction) is divided into two phases in Fig. 5, including the *kinetic-decrease* phase ($a-b$) and the *kinetic-increase* phase ($b-a^*$): in the *kinetic-decrease* phase, the kinetic energy $\langle E \rangle_\Omega$ decreases from the peak value a to zero b . As the $\langle E \rangle_\Omega$ goes to almost zero, each term on the left-hand side of Eq. (7) is equal to almost zero as well; in the *kinetic-increase* phase, the flow structure is reorganized, the kinetic energy gradually increases and gets to peak value again (a^*). The evolution of the flow structure is driven by multicontributions from elastic stress and thermal buoyancy in the different time ranges in the *kinetic-increase* phase. The elastic stress and the buoyancy work to increase kinetic energy in phases ($b-d$) and in phases ($c-a^*$), respectively.

To bring more clarity to the reversal process, we divide the *kinetic-increase* phase into three sub-phases by distinguishing the contributions that drive the flow, the phase of the *elastic-contribution* ($b-c$), in which only elastic stresses do positive work on the flow structure, the phase of the *elastic-buoyancy-contribution* ($c-d$), in which elastic stresses and thermal buoyancy act together with positive work on the flow structure; and the phase of the *buoyancy-contribution* ($d-a^*$), in

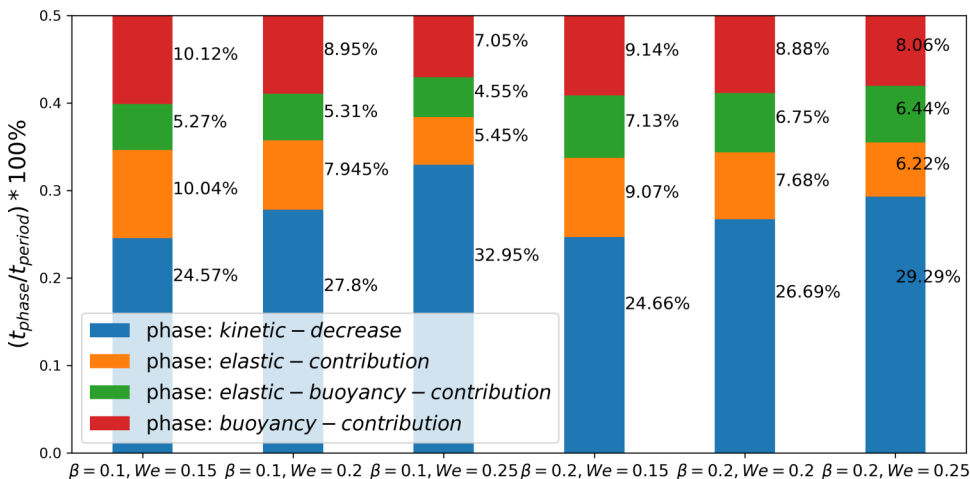


FIG. 7. Snapshots of normal stresses τ_{11} and τ_{22} at the five time points indicated in Fig. 5(a). The parameters are $Ra = 1200$, $Pr = 7.0$, $\beta = 0.1$, $We = 0.150$, $\epsilon = 0.1$, and $\xi = 0.05$.

which only thermal buoyancy does positive work on the flow structure. Note that a complete reverse period has two kinetic-energy periods, which differ only in the evolution of the velocity direction (from $u_2 > 0$ to $u_2 < 0$ or from $u_2 < 0$ to $u_2 > 0$).

The phase of *kinetic-decrease* starts at time-point a in Fig. 5(a) and ends at time-point b in Fig. 5(a), in which the global kinetic energy decreases from peak value a to zero (b). In this phase, the elastic energy exchange term $\langle \Phi_G \rangle_\Omega$ remains negative, which means the energy of the system is transformed from the kinetic energy into elastic potential energy, in other words, the kinetic energy is stored into polymer macromolecular structure. In addition, the buoyancy flux $\langle \Phi_F \rangle_\Omega$, that is the only generating term also decreases to zero resulting in the gradual vanishing of the velocity field. At the end of *kinetic-decrease* phase the high values of normal stresses (τ_{11} , τ_{22}) appear in the near-wall areas and along the vertical central line. This will be discussed further in Figs. 7(b) and 7(g). Two symmetric small vortices form and grow near the horizontal wall about the vertical centerline of the cavity when time passes time-point b [Figs. 5(c) and 5(d)].

The *elastic-contribution* and *elastic-buoyancy-contribution* phases are in the time range ($b-c$) and ($c-d$), respectively. At the start of the *elastic-contribution* phase, the velocity field almost stays stationary and buoyancy flux is also almost zero, but the magnitude of the elastic stress field is substantial, Figs. 7(b) and 7(g). At the beginning of the *elastic-contribution* phase, $\langle \Phi_G \rangle_\Omega$ changes from negative to positive, the kinetic energy slightly increases, but the buoyancy flux keeps going down to negative values $\langle \Phi_F \rangle_\Omega < 0$, which means that polymer structure starts doing positive work (contribution) on the flow structure. However, buoyancy distribution plays an inhibiting role in the flow convective process. The start of the reverse convection and its growth is initiated and supported in this phase by elastic stresses. The only positive-energy input (for flow structure) to drive the start of the opposite convection is the release of the elastic stress ($\langle \Phi_G \rangle_\Omega > 0$), especially normal stress τ_{22} (in the central region of the domain) and τ_{11} (in the near-horizontal wall) which offers enormous tensile force. The elastic energy of the polymer macro-molecular structure is transformed into the flow kinetic energy canceling out the dissipation effect of the negative buoyancy flux.

In the *elastic-buoyancy-contribution* phase, $\langle \Phi_F \rangle_\Omega$ changes its sign to be positive, both $\langle \Phi_F \rangle_\Omega$ and $\langle \Phi_G \rangle_\Omega$ contribute and accelerate the growth of the new vortices. Because both $\langle \Phi_F \rangle_\Omega$ and $\langle \Phi_G \rangle_\Omega$ are positive, the growth rate of the kinetic energy is significantly improved and a dissipating $\langle \Phi_V \rangle_\Omega$ is also found in this phase. The original vortices completely vanish and new vortices with opposite rotation take up all the domain in the *elastic-buoyancy-contribution* phase, Fig. 5(e).

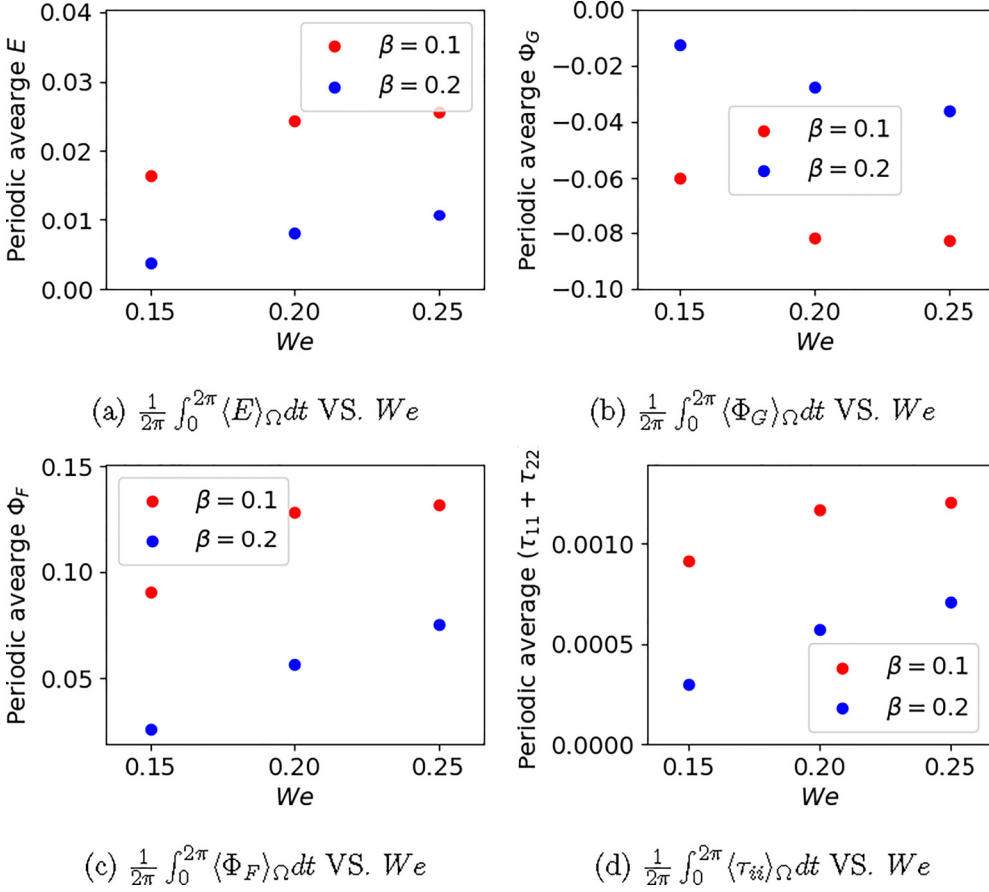


FIG. 8. Time proportion of each phase in one kinetic-energy period for $We \in (0.1, 0.15, 0.2)$ and $\beta \in (0.1, 0.2)$. The remaining parameters are fixed $Ra = 1200$, $Pr = 7.0$, $\epsilon = 0.1$, and $\xi = 0.05$. As the kinetic-energy period is only the half period of the convection reversal, the time ratio is based on the convection reversal period and the sum of the ratios is equal to 0.5. The period time for each case is remarked by red text in Fig. 6.

The *buoyancy-contribution* phase depicts the rapid increase of kinetic energy to the maximum value due to the formation of the new large-scale circulations. The flow structure is more efficiently driven by the buoyancy in this phase. In *buoyancy-contribution* phase ($b-a^*$ in Fig. 5), the elastic potential energy completes the role it played in the former two phases (initiation and acceleration reversals) and turns to absorbing energy from the flow structure in this phase, Fig. 6. The contours of the normal stresses (τ_{11} , τ_{22}) at key time points are shown in Fig. 7(d) [Fig. 7(e)] and Fig. 7(i) [Fig. 7(j)]. The increase in viscosity ratio β will reduce the time period while the increase in elastic strength We has the opposite effect.

Each phase in one whole reverse period for cases with $We \in (0.1, 0.15, 0.2)$ and $\beta \in (0.1, 0.2)$ is summarized in Fig. 8. We define time proportion of each phase by

$$\frac{t_{\text{phase}}}{t_{\text{period}}} \times 100\% \quad (10)$$

where t_{phase} is the time of each phase, t_{period} is the reversal time period of one flow reversal, which is remarked by red text in Fig. 6. The half period ($a-b-c-d-a^*$) is shown in the figure, as the time proportion of each phase in two half periods is the same. It can be clearly

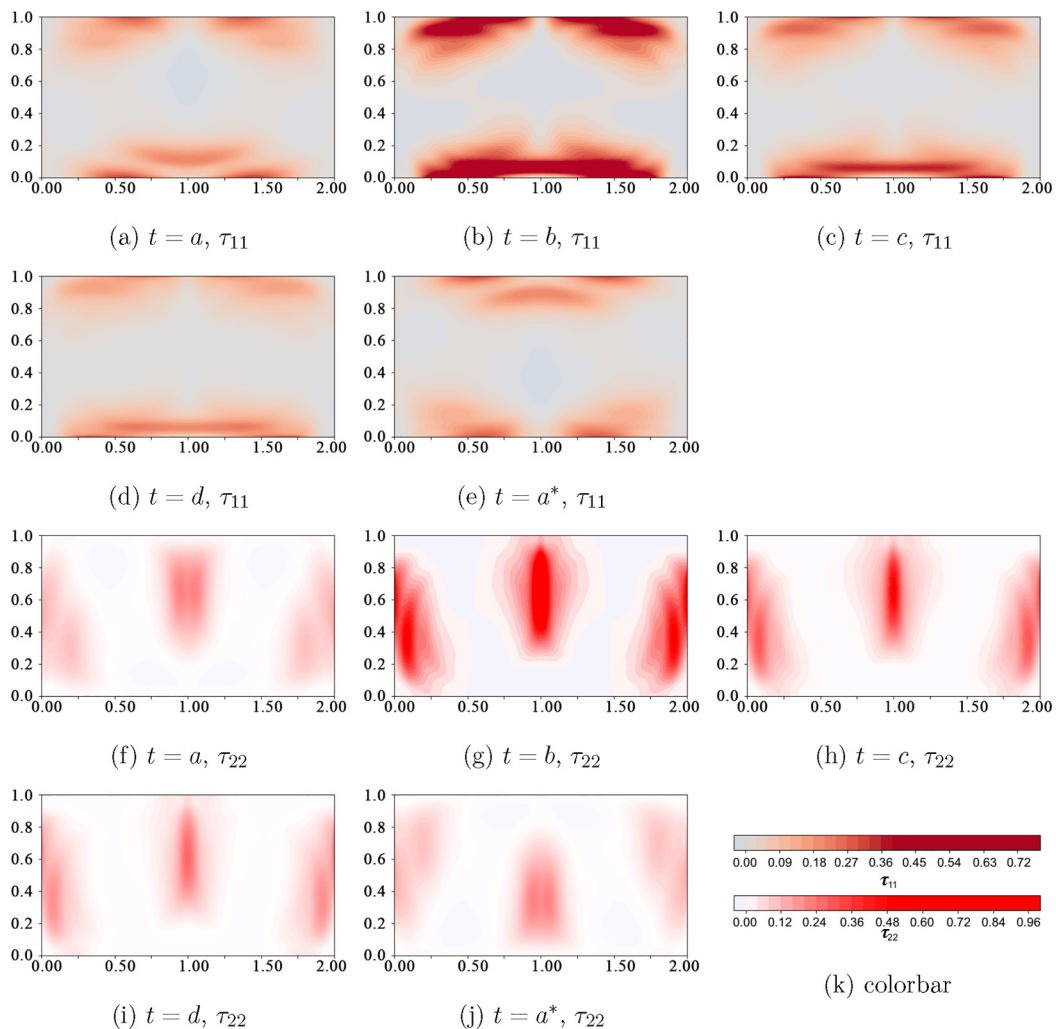


FIG. 9. (a) Averaged kinetic energy $\frac{1}{2\pi} \int_0^{2\pi} \langle E \rangle_{\Omega} dt$, (b) averaged energy exchange rate between flow structure and polymer $(\frac{1}{2\pi} \int_0^{2\pi} \langle \Phi_G \rangle_{\Omega} dt)$, (c) averaged buoyancy flux $(\frac{1}{2\pi} \int_0^{2\pi} \langle \Phi_F \rangle_{\Omega} dt)$, and (d) averaged elastic potential power intensity $(\frac{1}{2\pi} \int_0^{2\pi} \langle \tau_{11} + \tau_{22} \rangle_{\Omega} dt)$ as a function of We with $\beta \in (0.1, 0.2)$.

found that time proportion changes of each phase are almost monotonic relative to We and β . As We increases and β decreases, the time proportion of the *kinetic-decrease* phase is extended. This can be explained by the fact that, as the elastic effect increases in the reversal process, the macromolecular structure of the polymer can absorb and store more potential energy, and that it takes longer time for the energy to transfer from the flow structure to the elastic structure.

For higher We and smaller β , the stronger elastic effect means that elastic energy is released faster into the flow structure when the average kinetic energy of the velocity field is almost zero. The reversal process starts taking place at the very beginning of the *elastic-contribution* phase and continues in the *elastic-contribution* and *elastic-buoyancy-contribution* phases. In this phase elastic stress alone does positive work alone on the flow structure, and drives the reversal. The time proportion of the *elastic-contribution* and *elastic-buoyancy-contribution* phases is compressed as We increases and β decreases. Thus, elastic energy release takes less time to turn buoyancy flux

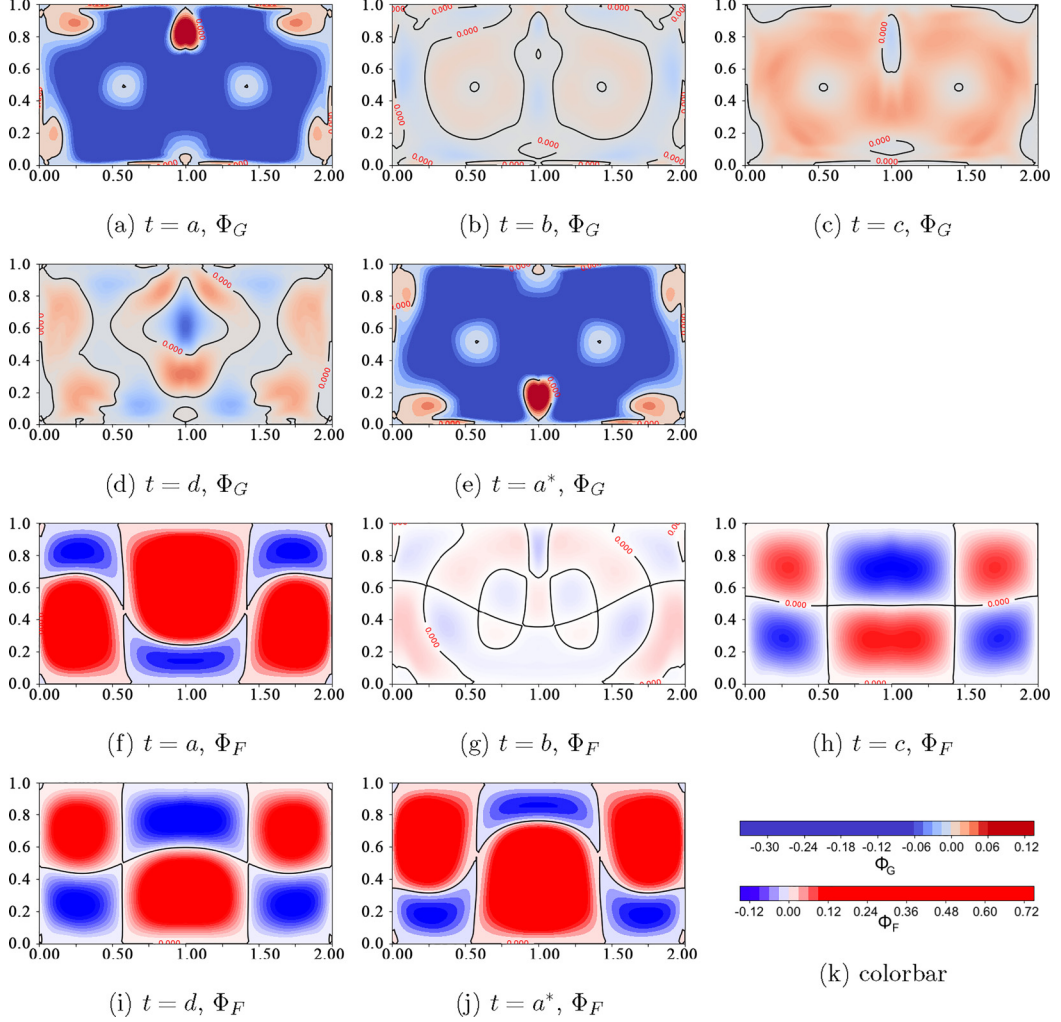


FIG. 10. The contours of Φ_G, Φ_F at five key time-points (a, b, c, d, a^*). The isoheight with zero value is drawn in Φ_G and Φ_F figures. In this case, $Ra = 1200, Pr = 7.0, \beta = 0.1, We = 0.150, \epsilon = 0.1,$ and $\xi = 0.05$.

to be positive. The latter increases rapidly and makes $\langle \Phi_G \rangle_\Omega$ turn to negative rather quickly. The time proportion of phase ($d-a^*$) also decreases with increasing We and decreasing β . It leads to a decrease in *kinetic-increase* phase for large We and small β .

Temporal-spatial averaged energies are also studied. Figure 9 shows the temporal-spatial averaged values of the kinetic energy (E), the energy exchange rate (Φ_G), the buoyancy flux (Φ_F) and the total normal elastic stress (τ_{ii}) as functions of We with different β . Under the same conditions, it is easy to find that these quantities increase with increasing We and decreasing β . Larger We and smaller β increases the kinetic energy and changes the convective flow.

C. Energy evolution in viscoelastic Rayleigh-Bénard convection from the local view

In this section, we shift our attention from spatial integrated variables to local distribution to see how each type of energy evolves in the reverse process to gain more insight into the reverse process. Figure 7 shows in detail the spatial distribution of the elastic normal stresses τ_{11} and τ_{22} , and Fig. 10

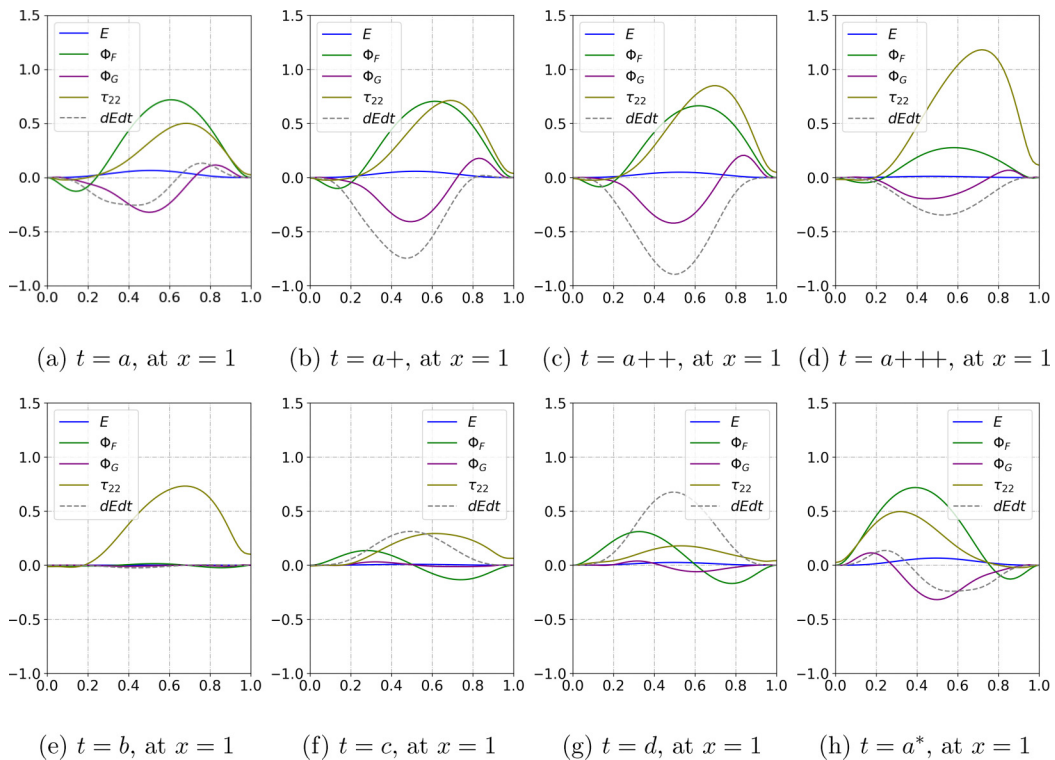


FIG. 11. Variation of the potential energies change along the central vertical line ($x = 1$). In this case: $Ra = 1200$, $Pr = 7.0$, $\beta = 0.1$, $We = 0.150$, $\epsilon = 0.1$, and $\xi = 0.05$. In the figures, $dEdt = \partial E / \partial t$ presents the partial derivative of momentum E with respect to time.

gives the detailed spatial distribution of the potential energies, including Φ_G and Φ_F , for $Ra = 1200$, $Pr = 7.0$, $\beta = 0.1$, $We = 0.150$, $\epsilon = 0.1$, and $\xi = 0.05$. Following Fig. 6, potential-energy contours are also drawn at five key time-points (a, b, c, d, a^*). Note that Figs. 5, 7, 10 correspond to the same time points [a, b, c, d, a^* ; marked in Fig. 5(a)]. The normal stresses, τ_{11} and τ_{22} , behave in an opposite manner; when one is maximum, the other reaches a minimum.

Figure 10 confirms that at the beginning of the *kinetic-decrease* phase ($t = a$), two symmetrical large circulations completely fill up the domain as shown in Fig. 5(b). At $t = a$, the elastic-kinetic-energy exchange term $\langle \Phi_G \rangle_\Omega$ is negative, but Φ_G is not negative everywhere in the cavity: the local maximum and minimum values take place about the vertical central line, as shown in Fig. 10(a). This indicates that kinetic energy is globally being either stored or dissipated in the polymeric structure and that the negative area fills most of the cavity as indicated by Fig. 10(a), but, at some places the kinetic energy is released into the flow. At the same time, the buoyancy flux ($\langle \Phi_F \rangle_\Omega > 0$) acts with positive work on the flow structure, but note that Φ_F is not positive everywhere in the cavity as shown in Fig. 10(f). We distinguish positive and negative zones separated by $u_2 = 0$ and $T = 0$ as $\Phi_F = Tu_2$.

Obviously the positive zones are larger than the negative ones: The central part near the bottom and the top parts near the cavity corners are negative zones indicating where Φ_F is a dissipating kinetic energy. From $t = a$ to $t = b$, the kinetic energy $\langle E \rangle_\Omega$ is reduced to almost zero. At $t = b$, $\langle E \rangle_\Omega = 0$ and the velocity field is zero everywhere in the cavity. $\langle \Phi_G \rangle_\Omega = 0$ and $\langle \Phi_F \rangle_\Omega = 0$ because u_2 is very weak and almost zero everywhere in the cavity. Positive zones of Φ_G appear at this time and behave as the source term of the kinetic energy: the kinetic energy increases very slowly from $t = b$ to $t = c$ confirming that $\langle \Phi_G \rangle_\Omega$ is the only positive source term to amplify the kinetic

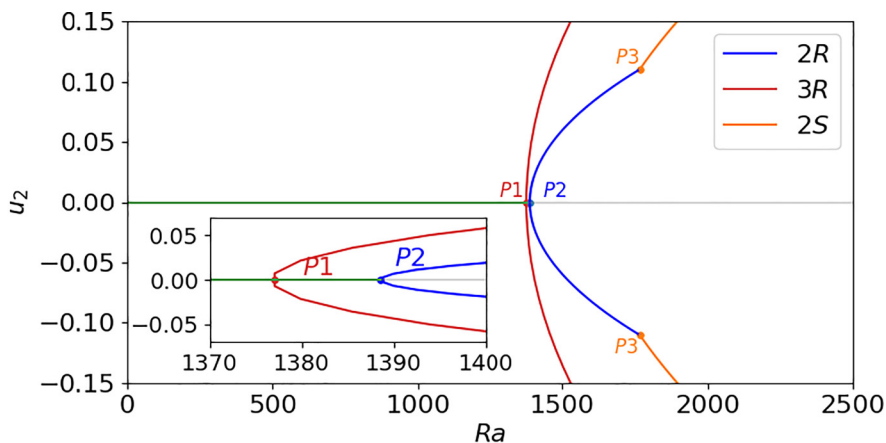
TABLE I. The flow condition with different Weissenberg numbers and Rayleigh numbers. In tested cases the following parameters are fixed: $Pr = 7.0$, $\beta = 0.2$, $\epsilon = 0.1$, and $\xi = 0.05$. In the table, R represents the reversal convection and S means the stable convection.

We	Ra	Cell number	Flow regime
0.07125	[1920, 1960, 2120, 2240, 2400, 2560]	2	R
	[1400, 1856, 1880, 1944, 2080]	2	S
		3	R
0.075	[1864, 1880]	2	R
	[1896, 2056, 2320, 2400]	2	S
	[1720, 1760, 1800, 1816, 1840, 1856, 1920, 2000, 2040, 2080, 2160, 2240]	3	R
0.1	[1400, 1480, 1560, 1680, 1760]	2	R
	[1800, 1920, 2080]	2	S
	[1424, 1504, 1584, 1664, 1744, 1824, 1904, 1984, 2064, 2144, 2224]	3	R
0.125	[1200, 1240, 1264, 1280, 1440, 1520, 1560, 1600, 1640, 1680]	2	R
	[1720, 1840]	2	S
	[1360, 1456, 1552, 1648, 1760, 1880, 2000, 2160, 2320]	3	R
0.150	[1040, 1120, 1136, 1200, 1280, 1360, 1440, 1520]	2	R
	[1616, 1696]	2	S
	[1216, 1296, 1376, 1456, 1584, 1680, 1840, 2000, 2080]	3	R
0.175	[960, 1040, 1240, 1320, 1400, 1520]	2	R
	[1560, 1600]	2	S
	[1296, 1456, 1616, 1696]	3	R
0.2	[880, 920, 976, 1080, 1200, 1360, 1440]	2	R
	[1480, 1512]	2	S
	[1136, 1296, 1456, 1616]	3	R
0.225	[840, 880, 1040, 1200, 1280, 1360]	2	R
		2	S
	[1136, 1296, 1456, 1616]	3	R
0.250	[800, 840, 976, 1080, 1200, 1240, 1280, 1320]	2	R
		2	S
	[1136, 1296, 1456, 1616]	3	R

energy from $t = b$ to $t = c$ and hence the velocity field. At $t = c$, $\langle \Phi_G \rangle_\Omega > 0$ and $\Phi_G = -u_{ij} \frac{\partial \tau_{ij}}{x_j} > 0$ takes place in most of the cavity because of $\tau_{ij} \frac{\partial u_i}{x_j}$ in the term Φ_G while $\langle \Phi_F \rangle_\Omega = 0$ is due to the symmetries observed in T (T is almost fully conductive) and u_2 . From $t = c$ the positive zones of Φ_F are growing and $\langle \Phi_F \rangle_\Omega$ becomes a positive source term of the kinetic energy and both $\langle \Phi_F \rangle_\Omega$ and $\langle \Phi_G \rangle_\Omega$ contribute to increasing the kinetic energy. At $t = d$, $\langle \Phi_G \rangle_\Omega$ is back to zero again and the positive zones of Φ_F become larger than the negative ones. From $t = d$, $\langle \Phi_F \rangle_\Omega$ is the only positive source term which increases the kinetic energy. As an auxiliary content to illustrate the evolution of reverse, and also for space reasons, the evolution of three-cell reverse is depicted in the Appendix.

Figure 11 shows the evolution of key variables (E , Φ_G , Φ_F , τ_{22} , and $dEdt$) along the y -direction line at $x = 1$ in a half period, where $dEdt = \frac{\partial E}{\partial t}$ presents the partial derivative of momentum E with respect to time. These variables play important roles in the reverse process as we have already discussed. The reason of selecting the line $x = 1$ for discussion is that E , Φ_F , τ_{22} , and Φ_G exhibit drastic changes during the reversal process.

E has its maximum at $t = a$, but the sign of $dEdt$ switches from negative to positive along the y direction, and is zero about $y = 0.63$, Fig. 11(a). That means there is an acceleration of E



(a) Bifurcation diagrams for VRBC.

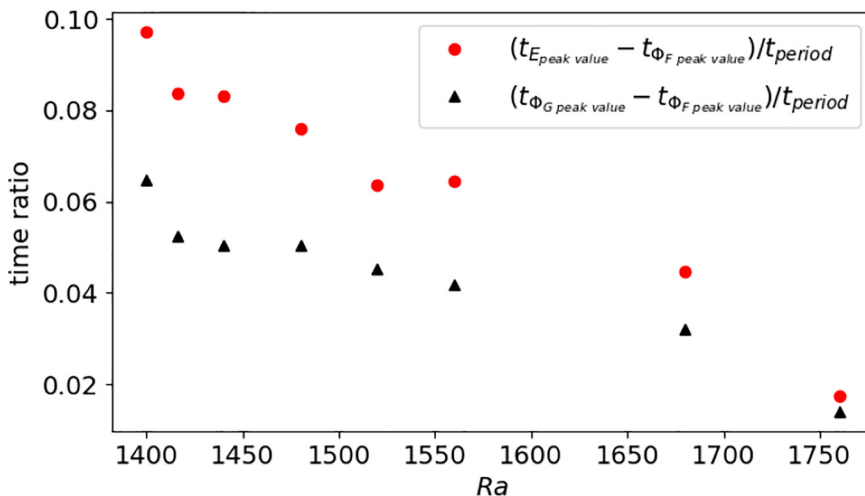

 (b) $R_{(\Phi_F, E)}$ and $R_{(\Phi_F, \Phi_G)}$ vs. Ra in $2R$.

FIG. 12. (a) Bifurcation diagrams showing the multiple flow patterns found in VRBC. The y-axis represents the y velocity at the monitoring point $(x, y) = (7/8, 1/2)$. (b) The time shift (delay) of peak value of (E, Φ_F) and (Φ_F, Φ_G) [$2R$ branch in panel (a)] as a function of Ra is shown. In the panel (b), $t_{E, \text{peak value}}, t_{\Phi_G, \text{peak value}}, t_{\Phi_F, \text{peak value}}$ are the time point when the peak value of $E, \Phi_F,$ and Φ_G take place in one period. The simulated cases correspond to $Pr = 7.0, \beta = 0.2, We = 0.1, \epsilon = 0.1,$ and $\xi = 0.05$.

starting from $y = 0.63$ up to $y = 1$ corroborated by the local $\Phi_G > 0$, Fig. 10(a). However, after $t = a$, as shown in Figs. 5(b) and 5(c), $dEdt$ becomes negative, meaning that E is decelerating, from $t = a+$ to $a+++$, and the local elastic stress τ_{22} increases rapidly, Figs. 7(f) and 7(g). That is to say that the time phase from $t = a+++$ to b , is a buffer area of the reversal system, because all variables in this time interval are decreasing. It is conceivable that during this time phase ($t = a+++$ to b), the absorption capacity of the macromolecular structure of polymer reaches a limitation, the elastic stress field becomes temporarily stagnant, and part of the elastic potential energy is released to the low-velocity region, but the E in the high-velocity region is still absorbed by the

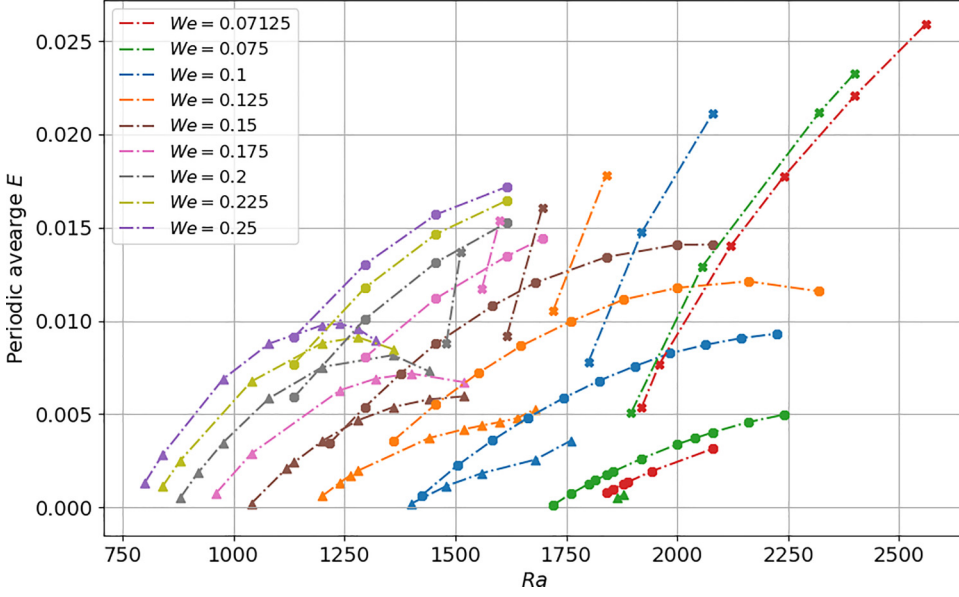


FIG. 13. Mean kinetic energy $E = \frac{1}{2\pi} \frac{1}{\Omega} \int_0^{2\pi} \int_0^{\Omega} (u_i u_i) dt dV$ as a function of Ra in VRBC, where the viscoelastic constitutive model is Phan-Thien-Tanner (PTT) model with $We \in [0.07125, 0.250]$ and $\beta = 0.2$. In the figure, (\bullet) means $3R$, (\blacktriangle) means $2R$, and (\times) means $2S$.

elastic stress field. Thus, Φ_G is negative and positive in the high-velocity and low-velocity areas, respectively, Fig. 10(b), which makes the velocity field more chaotic as shown in Fig. 5(c). Except τ_{22} , all potentials are almost zero at time $t = b$. In the interval $t = b$ to c , only elastic stress field τ_{22} plays its role, releases potential energy to the flow structure. The positive Φ_G almost fills the whole domain, Fig. 10(c). Buoyancy flux gradually plays a major role in the remaining time in the period to complete the reversal process, Figs. 10(i) and 10(j).

D. Effect of We on pattern selection

This section concerns the role of the elasticity, through the We values, on the flow patterns. Table I summaries the flow pattern of VRBC with different Ra and We . In this table, (S) represents the steady convection and (R) denotes the reversal convection. The constitutive parameters $\beta = 0.2$, $\epsilon = 0.1$, and $\xi = 0.05$ were fixed in all these simulations. We notice that the two-cells reversal convection does not take place when $We = 0.07125$. For cases with $We = 0.225$ and $We = 0.25$, two-cells steady convection was not obtained because the corresponding comprehensive elastic coefficient is too large, especially when β is small ($=0.2$) exceeding the solving ability of this solver. Convection is dominated by elasticity when β is relatively small.

Figure 12 depicts flow pattern selection in VRBC and the time shift (delay) of peak value of (E , Φ_F) and (Φ_F , Φ_G) as a function of Ra , which can more intuitively explain the reason of the periodicity of the transition from reversal to steady-state convection. Figure 12(a) plots the y velocity at the monitoring point $(x, y) = (7/8, 1/2)$ as function of Ra for cases with $Pr = 7.0$, $\beta = 0.2$, $We = 0.1$, $\epsilon = 0.1$, and $\xi = 0.05$. There are two (positive and negative) solution branches for convection pattern of $2R$ (two-cells) and $3R$ (three-cells). The positive and negative values of branches are maximum positive and negative velocities in one reversal period, respectively. Two time-dependent reversal convection branches $2R$ and $3R$ both start from the pure conduction state and distinguish from the different Hopf bifurcation $P2$ and $P1$, respectively, where $P1$ leads branch of $3R$, and $P2$ leads $2R$. With increasing Ra , another bifurcation $P3$, a drift pitchfork bifurcation,

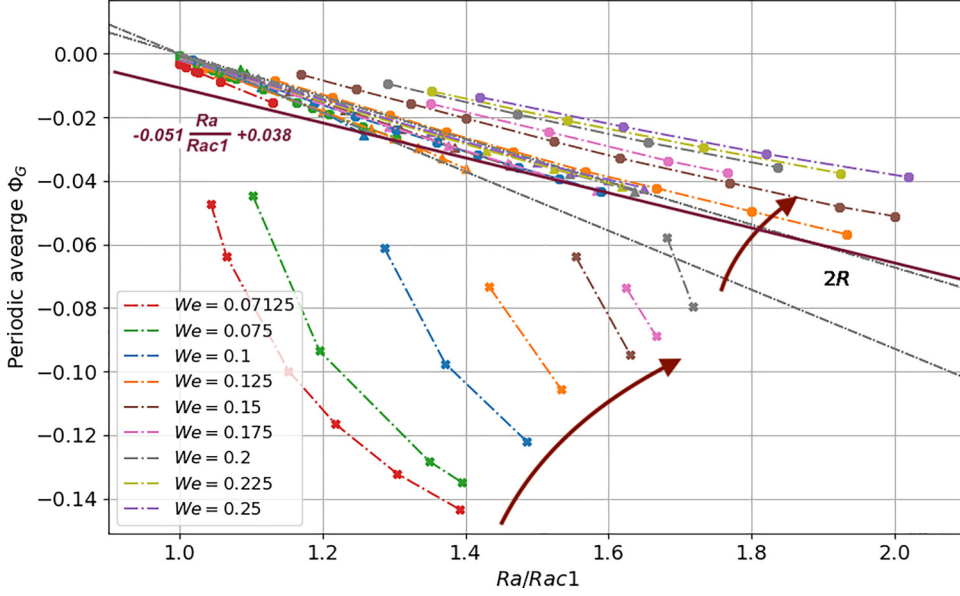


FIG. 14. Averaged energy exchange rate Φ_G as a function of Ra in VRBC, where the viscoelastic constitutive model is Phan-Thien-Tanner (PTT) model with $We \in [0.07125-0.250]$ and $\beta = 0.2$. In the figure, (●) means $3R$, (▲) means $2R$, and (x) means $2S$.

takes place on the branch of $2R$ and induces the flow transition from $2R$ to steady two-cell convection $2S$. For branches $3R$, when Ra exceeds a certain value, $3R$ will also transit to $2S$. But we do not very know the transit process from $3R$ to $2S$. It can be our next step.

In Fig. 12(b) is shown the time shift (delay) of the peak value of (E, Φ_F) and (Φ_F, Φ_G) as a function of Ra . Here, we define the time shift proportion by

$$R_{(E, \Phi_F)} = (t_{\Phi_F, \text{peak value}} - t_{E, \text{peak value}}) / t_{\text{period}}, \quad (11)$$

$$R_{(\Phi_F, \Phi_G)} = (t_{\Phi_G, \text{peak value}} - t_{\Phi_F, \text{peak value}}) / t_{\text{period}}, \quad (12)$$

where $t_{E, \text{peak value}}$, $t_{\Phi_F, \text{peak value}}$, $t_{\Phi_G, \text{peak value}}$ are the time point when the peak value of E , Φ_F and Φ_G take place in one period, as shown in Fig. 6. All tested cases in the figure are in the Ra region of regular reversal, and the flow state will change to steady convection as Ra further increases. It can be easily found that the time shift $R_{(E, \Phi_F)}$ and $R_{(\Phi_F, \Phi_G)}$ almost show the same decreasing trend as Ra increases, and when the Ra is close to $Rac2$, the $R_{(E, \Phi_F)}$ and $R_{(\Phi_F, \Phi_G)}$ (equivalent to $R_{(E, \Phi_G)}$) are almost be zero supporting our proposition that the formation of viscoelastic periodic reversal convection is due to the alternating transition of the system's total energy (kinetic energy, elastic energy, and buoyancy potential energy). The time phase difference between the appearance of different forms of energy (such as the maximum value) promotes this process. In other words, when the time phase difference ($R_{(E, \Phi_F)}$ and $R_{(\Phi_F, \Phi_G)}$) disappears, the flow pattern would have passed the bifurcation point $P3$ and the reversed convection would finally transit to steady-state convection.

Figure 13 shows the temporally and spatially averaged E as a function of Ra with different We . Several conclusions could be deduced from this figure:

(i) The rate of increase of the kinetic energy (vs Ra) is different for different flow structures. Among them, the steady-state flow has the highest growth rate of kinetic energy, represented by the cross symbol (x) in the figure.

(ii) As the Ra closes $Rac2$ (flow changes from $2R$ to $2S$), the average kinetic energy will decrease, we call this self-regulation.

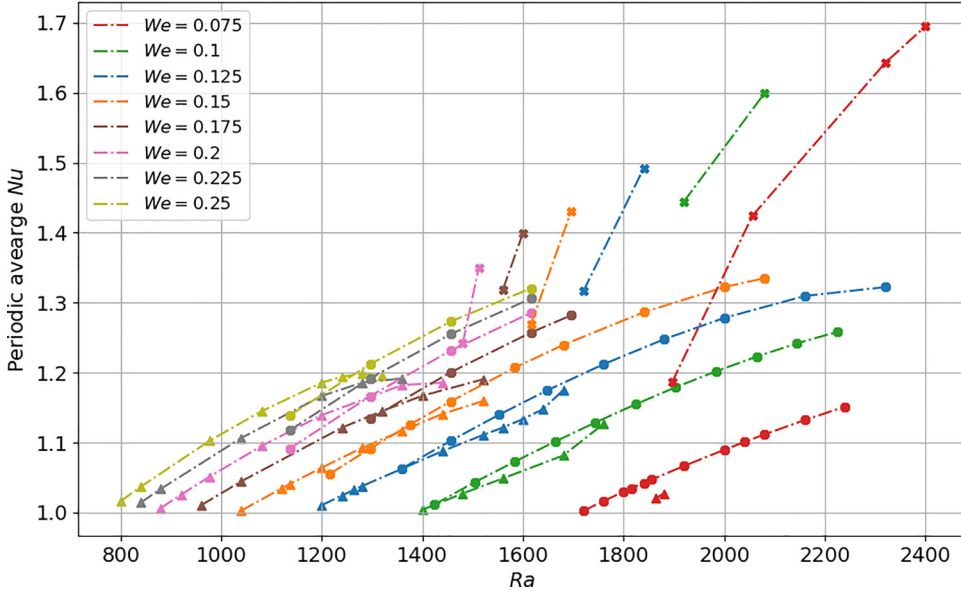


FIG. 15. Averaged Nusselt number Nu_{ts} as a function of Ra in VRBC, where the viscoelastic constitutive model is Phan-Thien-Tanner (PTT) model with $We \in [0.07125-0.250]$ and $\beta = 0.2$. In the figure, (●) means $3R$, (▲) means $2R$, and (×) means $2S$.

(iii) There is the overlap range of the Rayleigh number for two-cell and three-cell reversal condition.

(iv) No matter the initial flow state is two-cell or three-cell reverse convection, when the Rayleigh number exceeds the second critical number, the steady-state convection always has only two circulations.

In the same spirit, Fig. 14 shows the capacity of the energy exchange between the flow structure and the polymer macromolecular structure at different We , Ra , and flow condition. From Fig. 14, we can find that the overall energy exchange capacity of steady-state convection is stronger than that in reversed convection. The existence of the reversal phenomenon has a huge impact on the energy dissipation of the system. We can find a threshold of the energy exchange rate of Φ_G between

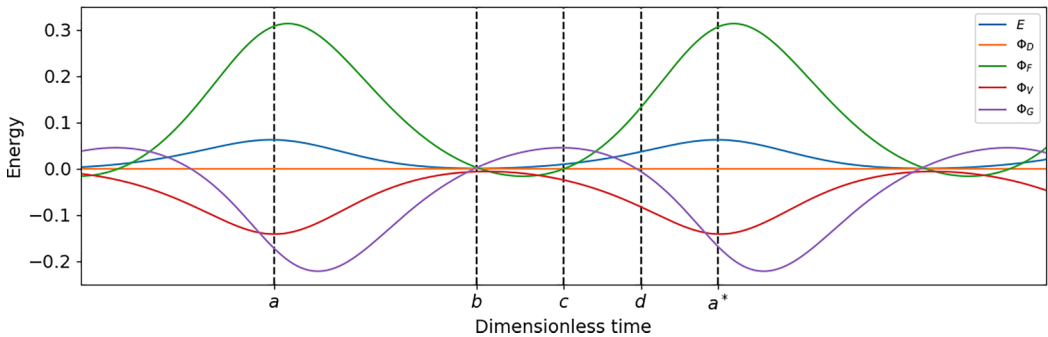


FIG. 16. Different averaged quantities as function of the dimensionless time in regular reversal convection system with three cells, where the rheological parameters are $\beta = 0.1$, $We = 0.15$, $Ra = 1200$, $\epsilon = 0.1$, and $\xi = 0.05$.

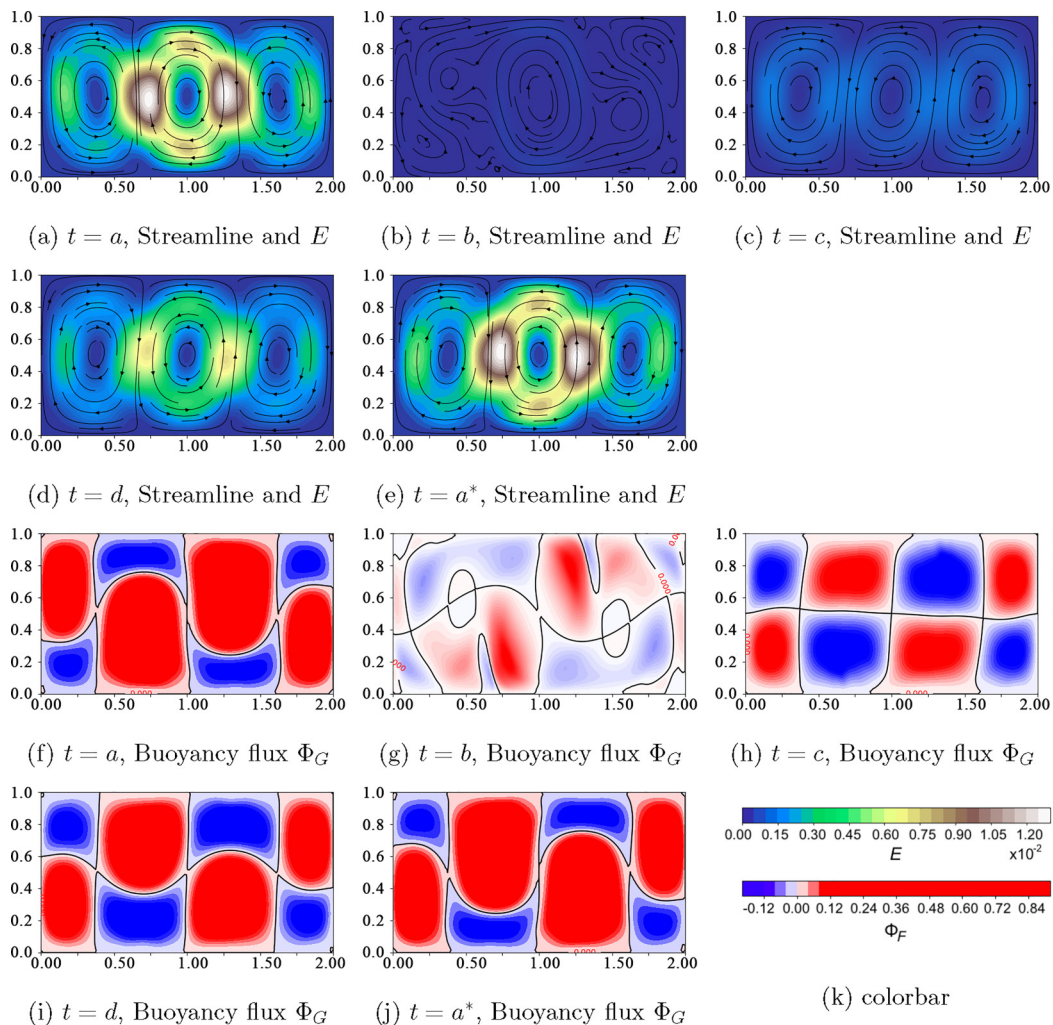


FIG. 17. The contours of the kinetic energy E and the buoyancy flux Φ_F at five key time-points (a, b, c, d, a^*). In the case we fixed parameters $Ra = 1200$, $Pr = 7.0$, $\beta = 0.1$, $We = 0.150$, $\epsilon = 0.1$, and $\xi = 0.05$.

reversal and stable convection. In present cases, this threshold obeys the function:

$$-0.051 \frac{Ra}{Ra_{c1}} + 0.038, \quad (13)$$

as shown in Fig. 14. The regular reversal convection only takes place when the Φ_G is under this value, and the flow pattern will change to stable convection once the Φ_G exceeds this value. The Φ_G shows a more of a linear relationship with Ra in the reverse region, compared with that in the steady convection region.

E. Heat transfer

The temporal-spatial averaged Nusselt number (Nu) as a function of Ra and We is plotted in Fig. 15. Nu is defined as the nondimensional temperature gradient at the bottom boundary of the

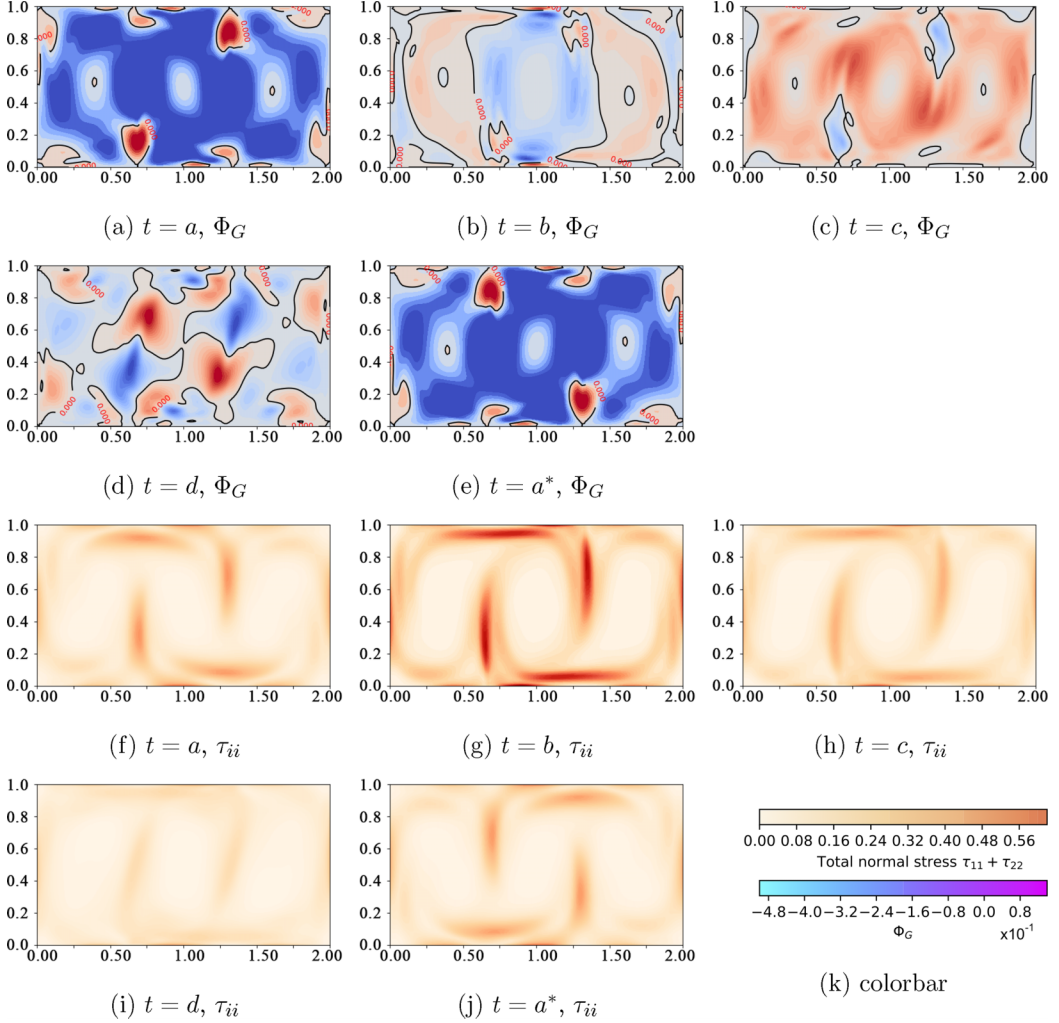


FIG. 18. The contours of Φ_G , total normal stress τ_{ii} at five key time-points (a, b, c, d, a^*). In the case we fixed parameters $Ra = 1200$, $Pr = 7.0$, $\beta = 0.1$, $We = 0.150$, $\epsilon = 0.1$, and $\xi = 0.05$.

cavity. The spatially temporally averaged Nusselt number Nu_{ts} is defined as

$$Nu_{ts} = \frac{1}{\lambda} \frac{1}{2} \int_0^\lambda \int_0^2 -\frac{\partial T}{\partial y} \Big|_{y=0} dx dt. \quad (14)$$

The behavior of Nu is similar to that of the kinetic energy shown in Fig. 13. It can be conversely found that under a certain Ra , the same convection system can have different flow states, reverse convection, or stable convection. For example when $We = 0.125$ and $Ra = 1750$, the flow state can be three-cell reverse convection or two-cell steady-state convection, depending on the previous flow mode. We can also observe that for the reversed convection state, the three-cell configuration is more stable than the two-cell configuration because the three-cell configuration can exist in a larger Ra range in Fig. 15.

From the perspective of heat transfer capacity, the growth rate of Nu in two-cell steady-state convection is much larger than that of the reverse convection, as described in Fig. 15. The reason

probably is in the flow process of reverse convection, the continuous stretching and contraction of the polymer structure in the system plays an intermittent obstructive effect on the flow.

IV. CONCLUSIONS

Two-dimensional numerical simulations of VRBC in a rectangular enclosure was performed in this paper. Time-dependent reversal convection onset in an enclosure of aspect ratio 2 : 1 was explored using an in-house-developed numerical code, covering the range of parameters $\beta = (0.1, 0.2)$, $We \in [0.007125, 0.25]$ and fixed $Pr = 7.0$. We note here that the viscoelastic fluid of the PTT type we worked with is highly elastic. As we had remarked earlier in Sec. II A the value $We = 0.1$ for the Weissenberg number in the present work is the equivalent of $We = 10.58$ in the work by Cheng *et al.* [9]. In the simulated VRBC cases a time-dependent flow, instead of a steady, exists during the convection with increasing We and decreasing β .

For time-dependent reversal convection, the evolution of the two-cell and three-cell flow structures were investigated in detail together with the energy conversion in the regular reversal convection and the elasticity effect on the promotion of the reversal formation. The potential energy in the convection system is periodically transported between the flow structure and the polymer. The flow is driven by an elastic force and thermal buoyancy. There is a critical value of the energy exchange rate Φ_G between periodically reversed convection and the steady-state convection. At higher Ra , time-dependent flow is replaced by a steady-state flow when another critical Rayleigh number ($Rac2$) is reached. This flow transition corresponds to a drift pitchfork bifurcation. The disappearance of the time-dependent convection is due to the gradual decrease or even disappearance of the time phase difference between the evolution of the elastic energy and the evolution of the velocity field with Ra .

The onset of the time-dependent reverse convection in the Rayleigh-Bénard convection with nonlinear viscoelastic fluids is a novel flow feature because of the particular flow patterns. These flow reversal characteristics are different and should not be confused with the random reversal in turbulent Rayleigh-Bénard convection.

ACKNOWLEDGMENTS

One of the authors, X.Z. thanks the Chinese Scholarship Council (CSC) for the financial support. Part of the results were obtained in the scope of PHC CAIYUANPEI project 44033SA.

APPENDIX: REVERSAL CONVECTION WITH THREE CELLS

To fully explain the mechanism of the viscoelastic property that drives the reversal convection, the kinetic-energy transport in the reversal convection system with three cells was also investigated. The same fixed parameters $Ra = 1200$, $Pr = 7.0$, $\beta = 0.1$, $We = 0.150$, $\epsilon = 0.1$, and $\xi = 0.05$ have been used to facilitate comparison with the two-cell configuration.

Figure 16 plots the different averaged terms (appearing in the kinetic energy) transport equation in the three-roll regular reversal convection versus dimensionless time. The time period for this case is $t = 0.92$, which is longer than that in the two-roll configuration ($t = 0.69$). Compared with the two-roll reversal convection, the evolutions in time of the different energies show behavior similar to that in Fig. 6. The five key time-points (a, b, c, d, a^*) are displayed in Figs. 17 and 18. Time point a marks the maximum of the kinetic energy and the minimum of the viscous dissipation, the maximum of the buoyancy flux $\langle \Phi_F \rangle_\Omega$ and the minimum of $\langle \Phi_G \rangle_\Omega$ occur later, but note that there is a slight delay between the extrema of $\langle \Phi_F \rangle_\Omega$ and $\langle \Phi_G \rangle_\Omega$. Time point b corresponds to the moment where $\langle E \rangle_\Omega$, $\langle \Phi_F \rangle_\Omega$ and $\langle \Phi_G \rangle_\Omega$ are equal to almost zero. At this particular time, $\langle \Phi_F \rangle_\Omega$ and $\langle \Phi_G \rangle_\Omega$ terms become a dissipation term instead of a production term and a kinetic-energy term instead of a dissipation term, respectively. At time point c , $\langle \Phi_F \rangle_\Omega$ is again zero. At b and c , $\langle \Phi_F \rangle_\Omega$ behaves as a dissipation term and after c both $\langle \Phi_F \rangle_\Omega$ and $\langle \Phi_G \rangle_\Omega$ behave as production terms. At

time-point d , $\langle \Phi_F \rangle_\Omega$ crosses zero again and retakes its role of a dissipation term. Between d and a^* , $\langle \Phi_F \rangle_\Omega$ is the only driving force to amplify to the kinetic energy and hence the velocity field.

The mechanism of the convection reversal is the following: before the time point a , the buoyancy flux $\langle \Phi_F \rangle_\Omega$ is increasing in time amplifying the kinetic energy and adding energy to the elastic reservoir; $\langle \Phi_F \rangle_\Omega$ reaches its maximum after the time-point a and continues to decrease whereas $\langle \Phi_G \rangle_\Omega$ reaches its minimum later. This delay in time makes the kinetic energy $\langle \Phi_F \rangle_\Omega + \langle \Phi_G \rangle_\Omega + \langle \Phi_V \rangle_\Omega + \langle \Phi_D \rangle_\Omega$ negative. The kinetic energy $\langle E \rangle_\Omega$ decreases, and is reduced to almost zero at time point b . The elastic potential plays the leading role as a production term after b and makes $\langle \Phi_G \rangle_\Omega$ to become positive again before retaking the dissipation role at time point d .

As observed in the two-cell case, at $t = a$ $\langle \Phi_F \rangle_\Omega$ is a positive term, but Φ_F displays local negative zones and at $t = b$ and c $\langle \Phi_F \rangle_\Omega$ is equal to zero because of $u_2 \approx 0$ at $t = b$ and the symmetries of T and u_2 at $t = c$. In the same way $\langle \Phi_G \rangle_\Omega$ is a dissipation term at $t = a$ but Φ_G displays local positive zones. In terms of the total normal stress, it remains globally positive: it is amplified from $t = a$ to b , and decreases from $t = b$ to $t = c$ and d . From $t = d$ to a^* , it is increasing again.

-
- [1] E. Bodenschatz, W. Pesch, and G. Ahlers, Recent developments in Rayleigh–Bénard convection, *Annu. Rev. Fluid Mech.* **32**, 709 (2000).
- [2] P. Manneville, *Dynamics of Spatio-Temporal Cellular Structures*, Springer Tracts in Modern Physics, Vol. 207 (New York, 2006).
- [3] A. Y. Gelfgat, Different modes of Rayleigh–Bénard instability in two- and three-dimensional rectangular enclosures, *J. Comput. Phys.* **156**, 300 (1999).
- [4] S. Bouabdallah, B. Ghernaout, M. Teggat, A. Benchatti, and F.-Z. Benarab, Onset of natural convection and transition laminar-oscillatory convection flow in Rayleigh–Bénard configuration, *Heat Technol. (Pisa, Italy)* **34**, 151 (2016).
- [5] D. Lohse and K.-Q. Xia, Small-scale properties of turbulent Rayleigh–Bénard convection, *Annu. Rev. Fluid Mech.* **42**, 335 (2010).
- [6] B. A. Toms, Some observations on the flow of linear polymer solutions through straight tubes at large Reynolds numbers, *Proc. of Int. Cong. Rheol.* **135** (1948).
- [7] M. Lappa and A. Boaro, Rayleigh–Bénard convection in viscoelastic liquid bridges, *J. Fluid Mech.* **904**, A2 (2020).
- [8] G. Ahlers and A. Nikolaenko, Effect of a Polymer Additive on Heat Transport in Turbulent Rayleigh–Bénard Convection, *Phys. Rev. Lett.* **104**, 034503 (2010).
- [9] J.-P. Cheng, H.-N. Zhang, W.-H. Cai, S.-N. Li, and F.-C. Li, Effect of polymer additives on heat transport and large-scale circulation in turbulent Rayleigh–Bénard convection, *Phys. Rev. E* **96**, 013111 (2017).
- [10] T. Green III, Oscillating convection in an elasticoviscous liquid, *Phys. Fluids* **11**, 1410 (1968).
- [11] C. M. Vest and V. S. Arpaci, Overstability of a viscoelastic fluid layer heated from below, *J. Fluid Mech.* **36**, 613 (1969).
- [12] H. Park and D. Ryu, Rayleigh–Bénard convection of viscoelastic fluids in finite domains, *J. Non-Newtonian Fluid Mech.* **98**, 169 (2001).
- [13] H. Park and K. Park, Rayleigh–Bénard convection of viscoelastic fluids in arbitrary finite domains, *Int. J. Heat Mass Transfer* **47**, 2251 (2004).
- [14] P. Siddheshwar, G. Sekhar, and G. Jayalatha, Effect of time-periodic vertical oscillations of the Rayleigh–Bénard system on nonlinear convection in viscoelastic liquids, *J. Non-Newtonian Fluid Mech.* **165**, 1412 (2010).
- [15] Y. Tasaka, K. Igaki, T. Yanagisawa, T. Vogt, T. Zuerner, and S. Eckert, Regular flow reversals in Rayleigh–Bénard convection in a horizontal magnetic field, *Phys. Rev. E* **93**, 043109 (2016).
- [16] A. Castillo-Castellanos, A. Sergent, and M. Rossi, Reversal cycle in square Rayleigh–Bénard cells in turbulent regime, *J. Fluid Mech.* **808**, 614 (2016).

- [17] P. Winchester, V. Dallas, and P. D. Howell, Zonal flow reversals in two-dimensional Rayleigh-Bénard convection, *Phys. Rev. Fluids* **6**, 033502 (2021).
- [18] I. Eltayeb, Nonlinear thermal convection in an elasticoviscous layer heated from below, *Proc. R. Soc. London, Ser. A* **356**, 161 (1977).
- [19] S. Rosenblat, Thermal convection in a viscoelastic liquid, *J. Non-Newtonian Fluid Mech.* **21**, 201 (1986).
- [20] H. Park and D. Ryu, Nonlinear convective stability problems of viscoelastic fluids in finite domains, *Rheol. Acta* **41**, 427 (2002).
- [21] Z. Li and R. E. Khayat, Finite-amplitude Rayleigh-Bénard convection and pattern selection for viscoelastic fluids, *J. Fluid Mech.* **529**, 221 (2005).
- [22] H. Hiromitsu, Overstability of a viscoelastic liquid layer with internal heat generation, *Int. J. Heat Mass Transfer* **29**, 645 (1986).
- [23] R. W. Kolkka and G. R. Ierley, On the convected linear stability of a viscoelastic Oldroyd-B fluid heated from below, *J. Non-Newtonian Fluid Mech.* **25**, 209 (1987).
- [24] H. Park and H. Lee, Hopf bifurcations of viscoelastic fluids heated from below, *J. Non-Newtonian Fluid Mech.* **66**, 1 (1996).
- [25] R. G. Larson, Instabilities in viscoelastic flows, *Rheol. Acta* **31**, 213 (1992).
- [26] J. C. Yang, T. Vogt, and S. Eckert, Transition from steady to oscillating convection rolls in Rayleigh-Bénard convection under the influence of a horizontal magnetic field, *Phys. Rev. Fluids* **6**, 023502 (2021).
- [27] J. Aurnou and P. Olson, Experiments on Rayleigh-Bénard convection, magnetoconvection and rotating magnetoconvection in liquid gallium, *J. Fluid Mech.* **430**, 283 (2001).
- [28] H. Park, K. Shin, and H. Sohn, Numerical simulation of thermal convection of viscoelastic fluids using the grid-by-grid inversion method, *Int. J. Heat Mass Transfer* **52**, 4851 (2009).
- [29] H. Park, Peculiarity in the Rayleigh-Bénard convection of viscoelastic fluids, *Int. J. Therm. Sci.* **132**, 34 (2018).
- [30] K. Kovalevskaya and T. Lyubimova, Onset and nonlinear regimes of convection of an elastoviscous fluid in a closed cavity heated from below, *Fluid Dyn.* **46**, 854 (2011).
- [31] B. Bhaduria and P. Kiran, Weak non-linear oscillatory convection in a viscoelastic fluid layer under gravity modulation, *Int. J. Non-Linear Mech.* **65**, 133 (2014).
- [32] P. Kolodner, Oscillatory convection in viscoelastic dna suspensions, *J. Non-Newtonian Fluid Mech.* **75**, 167 (1998).
- [33] C. Metivier, F. Brochard, M. Darbouli, and A. Magnin, Oscillatory Rayleigh-Bénard convection in elastoviscoplastic gels, *J. Non-Newtonian Fluid Mech.* **286**, 104428 (2020).
- [34] R. Benzi, E. S. C. Ching, and E. De Angelis, Effect of Polymer Additives on Heat Transport in Turbulent Thermal Convection, *Phys. Rev. Lett.* **104**, 024502 (2010).
- [35] D. Lyubimov, K. Kovalevskaya, and T. Lyubimova, Bifurcations in the problem of thermal convection of viscoelastic fluid in a closed cavity with free boundaries heated from below, *Appl. Nonlinear Dyn.* **19**, 16 (2011).
- [36] X. Zheng, M. Boutaous, S. Xin, D. A. Siginer, F. Hagani, and R. Knikker, A new approach to the numerical modeling of the viscoelastic Rayleigh-Bénard convection, in *ASME International Mechanical Engineering Congress and Exposition* (American Society of Mechanical Engineers, 2019), Vol. 59445, p. V007T08A027.
- [37] R. G. Larson, *Constitutive Equations for Polymer Melts and Solutions: Butterworths Series in Chemical Engineering* (Butterworth-Heinemann, 2013).
- [38] D. M. Shin, J. S. Lee, J. M. Kim, H. W. Jung, and J. C. Hyun, Transient and steady-state solutions of 2d viscoelastic nonisothermal simulation model of film casting process via finite element method, *J. Rheol. (Melville, NY, US)* **51**, 393 (2007).
- [39] X. Zheng, F. Hagani, M. Boutaous, R. Knikker, S. Xin, and D. A. Siginer, Pattern selection in Rayleigh-Bénard convection with nonlinear viscoelastic fluids, *Phys. Rev. Fluids* **7**, 023301 (2022).
- [40] F. Hagani, M. Boutaous, R. Knikker, S. Xin, and D. Siginer, Numerical modeling of non-affine viscoelastic fluid flow including viscous dissipation through a square cross-section duct: Heat transfer enhancement due to the inertia and the elastic effects, in *ASME International Mechanical Engineering Congress and Exposition* (American Society of Mechanical Engineers, 2020), Vol. 84584, p. V010T10A009.

- [41] Y.-K. Li, Z.-Y. Zheng, H.-N. Zhang, F.-C. Li, S. Qian, S. W. Joo, and L. V. Kulagina, Numerical study on secondary flows of viscoelastic fluids in straight ducts: Origin analysis and parametric effects, *Comput. Fluids* **152**, 57 (2017).
- [42] A. K. Townsend and H. J. Wilson, Small-and large-amplitude oscillatory rheometry with bead–spring dumbbells in Stokesian dynamics to mimic viscoelasticity, *J. Non-Newtonian Fluid Mech.* **261**, 136 (2018).